


# Emergence of Distinct Neural Subspaces in Motor Cortical Dynamics during Volitional Adjustments of Ongoing Locomotion

David Xing,<sup>1</sup> Wilson Truccolo,<sup>2,3</sup> and  David A. Borton<sup>1,3,4</sup>

<sup>1</sup>School of Engineering, Brown University, Providence, Rhode Island 02912, <sup>2</sup>Department of Neuroscience, Brown University, Providence, Rhode Island 02912, <sup>3</sup>Carney Institute for Brain Science, Brown University, Providence, Rhode Island 02912, and <sup>4</sup>Center for Neurorestoration & Neurotechnology, Rehabilitation Research and Development Service, Department of Veterans Affairs, Providence, Rhode Island 02908

The ability to modulate ongoing walking gait with precise, voluntary adjustments is what allows animals to navigate complex terrains. However, how the nervous system generates the signals to precisely control the limbs while simultaneously maintaining locomotion is poorly understood. One potential strategy is to distribute the neural activity related to these two functions into distinct cortical activity coactivation subspaces so that both may be conducted simultaneously without disruptive interference. To investigate this hypothesis, we recorded the activity of primary motor cortex in male nonhuman primates during obstacle avoidance on a treadmill. We found that the same neural population was active during both basic unobstructed locomotion and volitional obstacle avoidance movements. We identified the neural modes spanning the subspace of the low-dimensional dynamics in primary motor cortex and found a subspace that consistently maintains the same cyclic activity throughout obstacle stepping, despite large changes in the movement itself. All of the variance corresponding to this large change in movement during the obstacle avoidance was confined to its own distinct subspace. Furthermore, neural decoders built for ongoing locomotion did not generalize to decoding obstacle avoidance during locomotion. Our findings suggest that separate underlying subspaces emerge during complex locomotion that coordinates ongoing locomotor-related neural dynamics with volitional gait adjustments. These findings may have important implications for the development of brain–machine interfaces.

**Key words:** cortical dynamics; locomotion; motor control; neural subspaces

## Significance Statement

Locomotion and precise, goal-directed movements are two distinct movement modalities with known differing requirements of motor cortical input. Previous studies have characterized the cortical activity during obstacle avoidance while walking in rodents and felines, but, to date, no such studies have been completed in primates. Additionally, in any animal model, it is unknown how these two movements are represented in primary motor cortex (M1) low-dimensional dynamics when both activities are performed at the same time, such as during obstacle avoidance. We developed a novel obstacle avoidance paradigm in freely moving nonhuman primates and discovered that the rhythmic locomotion-related dynamics and the voluntary, gait-adjustment movement separate into distinct subspaces in M1 cortical activity. Our analysis of decoding generalization may also have important implications for the development of brain–machine interfaces.

Received Mar. 27, 2022; revised Oct. 10, 2022; accepted Oct. 12, 2022.

Author contributions: D.X., W.T., and D.A.B. designed research; D.X. performed research; D.A.B. contributed unpublished reagents/analytic tools; D.X., W.T., and D.A.B. analyzed data; D.X. wrote the paper.

This work was sponsored in part by the Defense Advanced Research Projects Agency (DARPA) BTO under the auspices of Dr. Doug Weber and Alfred Emond through the Space and Naval Warfare Systems Center Pacific or DARPA Contracts Management Office, Grant/Contract No. D15AP00112 (to D.A.B.); and by Merit Review Award #101RX002835 from the US Department of Veterans Affairs, Rehabilitation Research and Development Service (to D.A.B.). The contents of this manuscript do not represent the views of the Veterans Administration or the United States Government. The Department of Veterans Affairs did not provide any direct support for the animal work conducted for this project. We thank Ellen Xing for contributing to the creation of Figure 1 and Figure 2. We also thank the Pablo J. Salame Goldman Sachs endowed Associate Professorship of Computational Neuroscience at Brown University (to W.T.); and the Howard Reisman '76 Family Graduate Fellowship Fund, and the Charles A. Dana Graduate Fellowship Fund (to D.X.). These funding sources had no involvement in the design of this study, the collection or analysis of data, or the authorship of this manuscript.

The authors declare no competing financial interests.

Correspondence should be addressed to David A. Borton at david\_borton@brown.edu.

<https://doi.org/10.1523/JNEUROSCI.0746-22.2022>

Copyright © 2022 the authors

## Introduction

The nervous system is a highly flexible computational system capable of simultaneously performing many different functions. An emergent view on neural computation posits that networks of neurons engage in specific patterns of covariation for carrying out specific functions (Churchland et al., 2012; Kaufman et al., 2014; Elsayed et al., 2016; Gallego et al., 2018). By constraining these coactivation patterns to separate subspaces, which we will refer to as “neural modes,” the network is able to carry out computations associated with one function without interfering with the activity related to separate functions in the other subspaces (Fig. 1*b*). This allows for the same neural population to carry out multiple different processes. For example, to avoid prematurely activating downstream muscles during movement preparation,

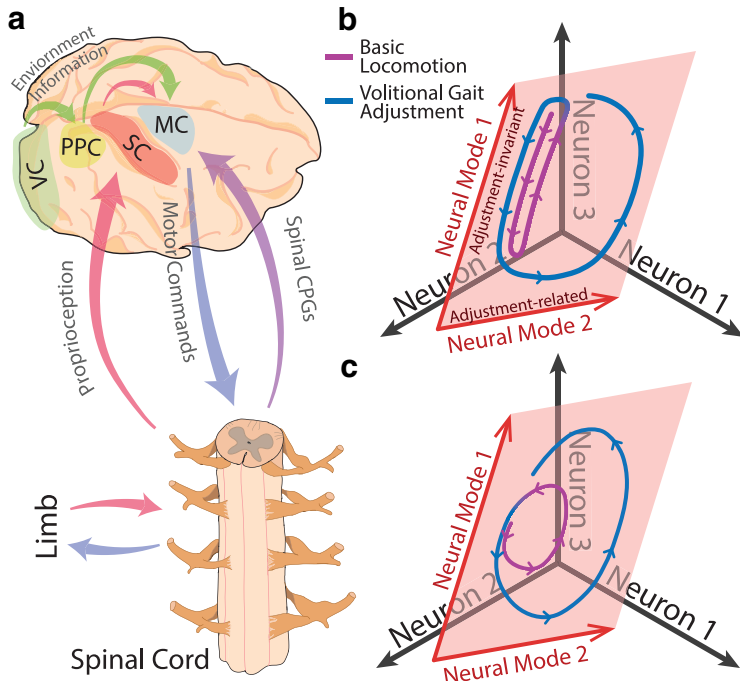


**Figure 1.** Neural modes related to volitional adjustments during locomotion. *a*, Schematic of pathways of some of the converging inputs onto motor cortex during volitional gait adjustments. Proprioception and spinal CPGs provide information about the limb position in the gait cycle while visual information from the environment both drives decision-making to react to complex environments and facilitates the calculation of the precise movement needed to successfully navigate the terrain. The nervous system must integrate all of these components to generate the appropriate motor command, which is relayed through the spinal cord to the limb. MC, Motor cortex; SC, somatosensory cortex; VC, visual cortex; PPC, posterior parietal cortex. *b*, *c*, Two possible strategies that the nervous system could use to carry out volitional gait adjustments. In this toy example, the full three-dimensional space represents all possible combinations of firing rates of three example neurons. The neural activity is confined to a two-dimensional subspace (red plane) spanned by two neural modes (red arrows). The curve represents the time-varying neural activity during one stride of basic locomotion (purple) followed by a stride with a volitional gait adjustment (blue). *b* represents the subspace-partitioning strategy that uses distinct neural modes to carry out certain functions, such as transmission of voluntary movement signals to downstream musculature. Here, the neural activity during basic locomotion is mostly confined to the first neural mode, while the second neural mode encodes the movement modifications. In *c*, which represents an alternative hypothesis, both neural modes are used during basic locomotion and both are modified by motor cortex during the volitional movement.

the neural variance in motor cortex resides primarily within an output-null neural subspace during the preparatory period, before transitioning into the distinct, output-potent subspace during movement (Kaufman et al., 2014). By separating or multiplexing the neural activity into distinct subspaces, the same network is able to engage in both movement preparation and movement execution. Additionally, the activity of primary motor cortex (M1) neurons in the same hemisphere corresponding to the left and right arms have also been shown to reside in orthogonal subspaces (Ames et al., 2019).

It is still unknown whether within movement execution itself, different types of movement performed simultaneously may also correspond to distinct subspaces. One particular behavior that may be amenable to the subspace separation hypothesis is locomotion. Previous studies have shown that the oscillator circuits responsible for basic locomotor movements reside in the spinal cord (Graham Brown, 1911; McCrea and Rybak, 2008), and that descending input from motor cortex is not required for carrying out unobstructed walking on a treadmill (Grillner et al., 1997). However, many animals have also developed the ability to precisely position their limbs in specific locations and orientations during locomotion, which facilitates navigation in

complex terrains (Georgopoulos and Grillner, 1989; Porter and Lemon, 1995; Beloozerova and Sirota, 1998; Yakovenko and Drew, 2015). During these behaviors, information about the environment is used to generate specific volitional movements that are integrated with the underlying locomotion rhythm. These volitional, gait-modifying movements are distinct from basic unobstructed locomotion, which consists of repeated rhythmic movements agnostic to the environment. Unlike in basic locomotion, motor cortex is essential for carrying out precise adjustments to the movements of the limb (Liddell and Phillips, 1944; Beloozerova and Sirota, 1998; Drew et al., 2002; Courtine et al., 2005) and must integrate top-down control of the muscles with information from sensory areas and the locomotor central pattern generator (CPG; Fig. 1*a*; Pruszynski et al., 2011; Scott et al., 2015). How M1 carries out the necessary computations to produce the correct volitional movement while also accounting for the underlying locomotion movements is poorly understood, especially in primates. One possibility could be that the neural population engages separate neural subspaces for tracking the basic cyclic rhythm and for carrying out the targeted, goal-oriented movements (Fig. 1*b*). This mechanism allows the same neural circuit to perform targeted, visually guided movements, such as those studied in center-out reaching paradigms, while at the same time preserving underlying walking movements during complex tasks such as walking across stepping stones or performing obstacle avoidance.

Here, we recorded neural activity from leg-M1 in freely moving nonhuman primates while they performed basic locomotion as well as stepping over an incoming obstacle on a treadmill. We found that locomotion movements, as well as volitional, gait-adjusting movements are represented in the same recorded neural population. Using dimensionality reduction, we found underlying neural modes that are completely unaffected by the obstacle avoidance movement, despite large changes in the kinematics. Separate neural modes captured the variance in the population activity that encoded the obstacle avoidance movement. Therefore, M1 appears to engage two distinct subspaces, one for accounting for the ongoing cyclic dynamics present during locomotion, and one for controlling the momentary change in M1 engagement during the gait modification.

## Materials and Methods

**Animal husbandry.** All experimental and surgical procedures were performed under approved Institutional Animal Care and Use Committee protocols at Brown University. Two male rhesus macaques, which were 7 and 9 years of age, were housed in individual cages and trained to perform the obstacle avoidance walking task. Positive reinforcement in the form of solid food was used.

**Experimental design.** All behavioral tasks were conducted inside a treadmill enclosure. The treadmill was purchased commercially (Jog A Dog), and a custom Plexiglas box (length, 177.8 cm, width, 47.6 cm; height, 91.4 cm) was constructed above it (Fig. 2*a*). Similar to previous recording studies (Foster et al., 2014; Yin et al., 2014; Berger et al., 2020), animals were able to move freely inside the enclosure and were not tethered in any way. To encourage consistency of movements across trials

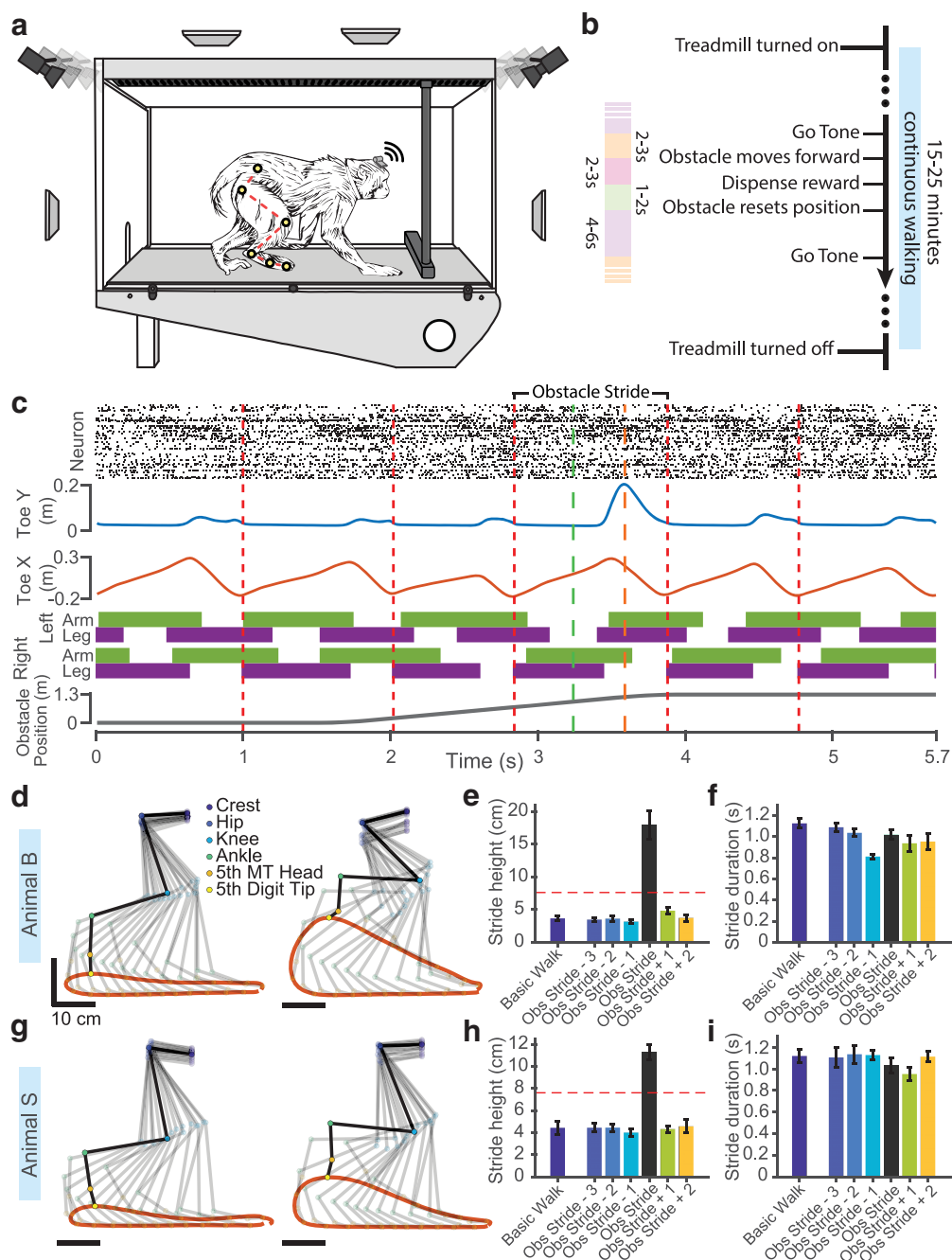


**Figure 2.** Experimental paradigm and behavior. **a**, Treadmill enclosure where animals performed locomotion and obstacle (Obs) stepping. Antennas surrounding the enclosure wirelessly collected neural data while video cameras recorded the positions of six joint markers painted on the hindlimb. **b**, Behavioral paradigm. Each trial consisted of a single obstacle run. **c**, Example data from a single trial of animal B, showing the stride bringing the leg over the obstacle along with three strides before and two strides after the obstacle stride. Top, Raster plot from the implanted leg-M1 microelectrode array. Blue trace, Height of the right toe tip; orange trace, horizontal position of the right toe tip. Second to bottom, Gait pattern across all four limbs. Solid bars, stance phase; purple, hindlimbs; green, forelimbs. Bottom, Obstacle position along the path of the treadmill. Dotted red lines demarcate the start of each gait cycle, green and orange lines indicate when the leading and lagging hindlimbs crossed over the obstacle respectively. **d, g**, Stick diagram of the right hindlimb during one stride of basic, unobstructed walking (left) or during one stride stepping over the obstacle (right). Orange trace represents the trajectory of the toe tip. Stick figures are spaced 60 ms apart, with the dark stick figure highlighting the limb during the maximum height of the toe tip. **e, h**, Maximum height reached by the toe tip for either unobstructed (basic) walking or the stride over the obstacle and the surrounding strides. Error bars represent SD. Dotted red line, Height of the obstacle. **f, i**, Duration of each stride, error bars are SD. **d–f**, Animal B; **g–i**, animal S.

and also to protect the obstacle components of the apparatus, Plexiglas walls were placed below the ceiling and in front of the animal, removing 43.8 cm of the top of the enclosure and 72.4 cm of the front of the enclosure from the available space that the animals were able to move in (not depicted in Fig. 2).

A 5.08-cm-high by 4.45-cm-wide by 42.86-cm-long rectangular Styrofoam bar served as the obstacle. The bar was attached to a stepper motor, which rotated the obstacle into and out of the path of the animal.

The motor was attached to a belt linear actuator (Igus), which moved the obstacle back and forth along the length of the treadmill. The obstacle apparatus was attached to the ceiling of the treadmill enclosure such that the top of the obstacle bar was 7.62 cm above the treadmill floor. Additionally, a speaker was placed in the ceiling to play audio tones, and a small slot in the front of the enclosure allowed food rewards to be placed on the treadmill belt and carried to the animal. Treadmill speed, obstacle speed, and timing of the audio tones were measured

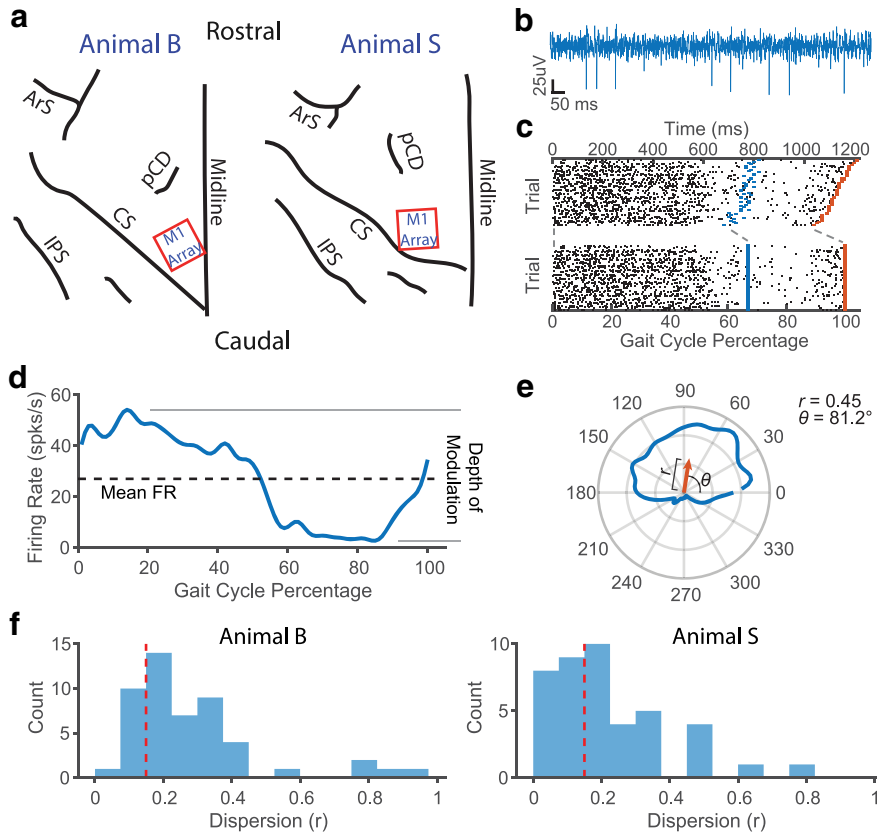


**Figure 3.** Neural recording and processing. *a*, Microelectrode array implant locations. Red rectangles indicate where the Utah arrays were implanted in the leg-area of M1 in the left hemisphere. ArS, Arcuate sulcus; pCD, pre-central dimple; CS, central sulcus; IPS, intraparietal sulcus. *b*, Example recording from one of the implanted electrodes. *c*, Example raster of the spiking activity of a neuron from animal B across multiple trials normalized to the gait cycle. Blue lines indicate foot-off time points (stance to swing transitions), and orange lines indicate foot-contact time points (swing to stance transitions). *d*, PETH of the spiking activity of a neuron shown in *c* after normalization. Dotted black line indicates the average firing rate across the gait cycle, and depth of modulation is calculated as the difference in the minimum and maximum firing rate across the gait cycle. *e*, The PETH in *c*, but shown as a polar plot. Circular statistics were used to calculate the average directional vector (orange arrow). The magnitude of the vector is the dispersion,  $r$ , of the neuron, and the angle,  $\theta$ , is the preferred phase of the neuron. *f*, Distribution of dispersion values for the whole recorded population of neurons for animal B (left) and animal S (right). Dotted red line at the value of 0.15 separates the weakly ( $<0.15$ ) and strongly ( $>0.15$ ) modulated neurons.

using a hall-effect angular position sensor, stepper quadrature encoder, and electret microphone, respectively.

Eight cameras were positioned around the enclosure and captured video of the animals performing the tasks at 100 Hz (SIMI Reality Motion Systems). Camera calibration was performed after each recording session to determine the positions and angles of each camera relative to each other, allowing for 3D triangulation of any markers that appear in at least two cameras. UV floodlights were placed around the recording room to enhance the visibility of our UV reactive joint markers (see Kinematics). The cameras were synchronized to each other and to the neural data with TTL (transistor–transistor logic) sync pulses. Additionally, 16 radiofrequency antennas were placed above and around the treadmill enclosure to receive the neural data transmitted through our wireless headstage (Fig. 2*a*).

The video capture was controlled through the Simi Motion software, and the neural data capture was controlled through Central software (Blackrock Microsystem). The treadmill, obstacle, and audio tone playback were controlled through a custom C++ program.

**Behavioral tasks.** Animals performed either basic unobstructed locomotion by walking on the treadmill without any other interactions or obstacle avoidance by stepping over an incoming obstacle during walking. Each of these tasks was conducted in blocks. Before entering the treadmill enclosure, animals were trained to enter a primate chair, which allowed us to attach the wireless recording headstages (Cereplex W, Blackrock Microsystems). The fur on the hindlimb was shaved, and the joint markers were also painted on at this time. Animals were then

allowed to enter the treadmill enclosure where they were able to move freely.

During obstacle avoidance blocks, the treadmill was first turned on at 2.2 km/h. The obstacle would be in position in the front of the treadmill, but fixed for 1 min to allow the animals to settle into a natural walking rhythm. At the start of each trial, a “go” tone was played to indicate that the obstacle was about to move. The operator would wait for a specific point in the gait cycle, contact of the right forelimb with the ground, before starting the obstacle movement. The obstacle would move forward at 2.2 km/h until it was past the animal, and then rotate up out of the way of the animal. The obstacle was then moved back to the front of the treadmill and rotated down into the path of the animal to assume the starting position for the next trial. After stepping over the obstacle, and while it was moving back into position, a “success” tone was played and a food reward was placed in the front of the treadmill, which would be carried by the moving belt to the animal. After a few seconds to allow the animal to eat the reward and resume normal walking, the go tone would play again to initiate the next trial (Fig. 2*b*). At the end of the obstacle avoidance block, the treadmill would be turned off.

During basic walking blocks, the treadmill would be turned on and the animal would walk continuously without any obstacle or food interaction for 2–5 min. We would also include some of the strides at the beginning of the obstacle avoidance block before the obstacle was moved for the first time as basic walking trials. We excluded the first two strides after the treadmill was turned on and the last two strides before the treadmill was turned off to avoid any transition effects. All animals were trained to proficiently step over the obstacle without hitting it before experimental recordings were initiated.

**Surgery.** All surgical procedures were performed under general anesthesia induced through isoflurane. Animals were sedated with ketamine (15 mg/kg) and midazolam (0.05 mg/kg), and given buprenorphine (0.01 mg/kg) preoperatively and intraoperatively. Buprenorphine SR (sustained release; 0.2 mg/kg) and meloxicam (0.2 mg/kg) were administered postoperatively. A craniotomy was performed, and 96-channel multielectrode arrays (Blackrock Microsystems) were inserted into the left leg area of M1 (leg-M1), which was identified via cortical landmarks (Fig. 3*a*). These implants were well within the regions demarked from anatomic tracing studies (He et al., 1993). Electrodes were platinum, 1.5 mm in length, and attached to a percutaneous pedestal that was fixed to the skull. Animals were given at least 1 week to recover after the implantation surgery before resuming the behavioral tasks.

**Kinematics.** We used UV-reactive colored body paint to mark the positions of six joints of the right hindlimb. We identified the joints through bony landmarks and painted circular markers over the iliac crest (crest), greater trochanter (hip), femur lateral epicondyle (knee), lateral malleolus (ankle), fifth metatarsal head (knuckle), and fifth distal phalanx (toe). Multicamera video tracking was used to determine the 3D position of each of the joints (SIMI Reality Motion Systems). The direction of the treadmill movement was determined through markers placed on the side of the treadmill, and the kinematics axes were rotated so that the  $x$ -axis corresponded to the direction of walking, the  $y$ -axis corresponded to the height, and the  $z$ -axis corresponded to medial–lateral movement. Because the animals were able to freely move back and forth



along the length of the treadmill, we normalized the  $x$ -position of each of the joints to the  $x$ -position of the iliac crest.

Additionally, the timing of gait events (e.g., right hand off, left foot strike) were obtained manually by inspecting the video and marking the frame when the event occurred. A stride was defined as the time from one heel-strike of the limb to the next heel strike; the stance phase was defined as the period from the first heel-strike to the next toe-off, while the swing phase was defined as the toe-off to the next heel-strike.

**Neural data processing.** Intracortical recordings were obtained at 30 kHz, bandpass filtered (300–3000 Hz), and thresholded to  $4\times$  the SD for spike events. Spikes  $>1000\ \mu\text{V}$  in amplitude were rejected as noise. For each channel, we used Wave Clus superparamagnetic clustering to semiautomatically extract waveform templates (Quiroga et al., 2004), and used subtractive waveform decomposition for automated template matching of the thresholded spikes (Vargas-Irwin and Donoghue, 2007). We were able to isolate 50 neurons from animal B and 42 neurons from animal S. Spike counts were obtained by binning the number of spike events into 10 ms bins corresponding to each frame of the video data. Single-trial smoothed firing rate values were computed by convolving with a Gaussian kernel (SD, 40 ms).

Because each stride could vary in length, to compare across strides, we normalized the neural and kinematic data to the gait cycle. The start of the stride (heel-strike) was defined to be 0%, the toe-off frame of each stride was defined to be the average duty factor, and the end of the stride (next heel-strike) was defined to be 100%. We used piecewise-linear time warping to interpolate the data at each percentage point from 0% to 100% (MATLAB *interp1()* function; Fig. 3c). Perievent time histograms (PETHs) were computed by averaging the normalized spike counts across trials and then smoothed with a Gaussian kernel (SD, 20 ms). Because of the unconstrained movement of the animals and wireless transmission of neural data, there would be periods where none of the antennas were able to receive the signal from the headstage. We excluded trials from analysis if  $>5\%$  of the time points contained a dropped signal.

**Neural response characterization.** Because the strides are cyclical, we used circular statistics to characterize the response profiles of each neuron (Drew and Doucet, 1991; Berens, 2009). The circular mean vector of the PETH was calculated by representing each value of the PETH as a polar vector and averaging across all percentage points (Fig. 3e). The preferred phase of the neuron was defined as the angle of the mean vector, while the dispersion was defined as the magnitude. The depth of modulation was calculated as the difference between the maximum and minimum firing rate of the PETH, and the mean firing rate was calculated as the average firing rate across all of the gait percentages. To identify neurons whose activity was uniform across the gait cycle, we applied the Rayleigh test at  $\alpha = 0.05$  with Bonferroni's correction for multiple testing. We classified neurons as multimodal if there were more than one peak that was  $>50\%$  of the depth of modulation for  $>10\%$  of the gait cycle. Finally, we classified neurons as strongly modulated if they had a dispersion value  $>0.15$ . Since the preferred phase is only well defined for neurons that are both significantly modulated to the gait cycle and have a unimodal PETH, we excluded neurons that are multimodal or weakly modulated from preferred phase calculations (but not depth of modulation or mean firing rate calculations). All processing was done in MATLAB with the Circ-stat toolbox.

To quantify the magnitude of change in the kinematics and neural activity during the obstacle stride, we calculated the Mahalanobis distance between the signal during the obstacle stride and the signal during the stride before any obstacle movement (three strides before the obstacle stride), which served as the baseline reference. At each gait percentage of the reference stride, we obtained the intertrial distribution of the neural or kinematic activity in 15-dimensional space. For kinematics, this constituted the three spatial positions of the hip, knee, ankle, knuckle, and toe. For neural data, using the full 50- or 42-dimensional neural space resulted in singular matrix issues, so we instead used the top 15 dimensions after performing principal component analysis (PCA) on the neural firing rates. After obtaining the mean and covariance matrix of this reference distribution, the Mahalanobis distance was computed for each trial of the obstacle stride at that gait percentage. The

distance was calculated for all percentages of the gait cycle. The average and SD of the distances across trials is seen in Figure 5,  $k$  and  $l$ . We also computed the cross-correlation between the average Mahalanobis distance of the neural activity and the average distance of the kinematics at various time lags ranging from  $-20$  to  $20$  gait percentages. We used the MATLAB functions *mahal()* and *crosscorr()* to implement the analyses.

**Demixed principal component analysis.** We wanted to test the hypothesis that separate underlying neural modes are used to carry out basic locomotion and to carry out volitional, target-directed movements, such as lifting a limb over the obstacle. We expect to find distinct, nonoverlapping subspaces, such as those shown in Figure 1b, if this hypothesis is correct. Alternatively, we may find largely the same subspaces corresponding to both nonobstructed locomotion and to the volitional obstacle avoidance movement, such as shown in Figure 1c, which would not support the subspace-partitioning hypothesis. We took two complementary approaches to test this hypothesis, using both supervised and unsupervised methods to model the low-dimensional neural modes (see Fig. 6). We used demixed PCA (dPCA) to find task-specific subspaces within the population activity (Kobak et al., 2016). dPCA is similar to PCA in that they are both linear dimensionality reduction methods that project high-dimensional time series data into a lower-dimensional space via a “decoder” matrix. For a set of task-specific PETHs (one for each neuron), we used the following:

$$\mathbf{X} = \mathbf{B}\mathbf{Y}, \quad (1)$$

where  $\mathbf{Y}$  is a  $n \times p$  matrix representing the mean-subtracted PETHs of  $n$  neurons at  $p$  samples/datapoints;  $\mathbf{X}$  is the  $m \times p$  matrix of the activity of  $m$  latent dimensions, with  $m < n$ ; and  $\mathbf{B}$  is the  $m \times n$  decoder matrix that projects each of the  $n$  dimensions to the lower  $m$ -dimensional space. (We note that in the following we will use the same letters/symbols to denote different but analog variables, whose specific meaning should be clear from the context.)

We refer to each of the  $m$  variables as a latent dimension or neural mode. However, unlike PCA, which finds the projection that maximizes the variance accounted for (VAF) by each of the  $m$  dimensions regardless of any task-related parameters, dPCA attempts to find task-related subspaces. The study by Kobak et al. (2016) provides an in-depth walk-through of the dPCA algorithm and implementation. We applied the MATLAB toolbox supplied by Kobak et al. (2016) for all our dPCA calculations.

For our data, we chose to use the following two task parameters: gait cycle percentage, which, in the unnormalized case, would correspond to time, and stride type. Gait cycle percentage varied from 0% to 100% and stride type varied from three strides before the obstacle stride to two strides after. We combined stride type and stride percentage interaction terms into the stride type marginalization, since we expect the stride-related neural activity to also be time varying. Therefore, the gait percentage marginalization subspace, which we call the stride-invariant subspace, should only vary with the gait cycle percentage and not with the stride type, while the stride marginalization subspace, which varies with both gait percentage and stride type, will be our stride-dependent subspace. We therefore are able to split the decoder matrix into the following two separate matrices:

$$\mathbf{B} = \begin{bmatrix} \mathbf{D}_{\text{inv}} \\ \mathbf{D}_{\text{dep}} \end{bmatrix}, \quad (2)$$

where  $\mathbf{D}_{\text{inv}}$  represents the decoder matrix that projects the neural activity to the subspace that is invariant to the stride type, and  $\mathbf{D}_{\text{dep}}$  represents the decoder matrix that projects the neural activity to the subspace that varies with the stride type. In addition to the two decoder matrices, dPCA finds the two corresponding encoder matrices that project the low-dimensional neural modes back to the high-dimensional space,  $\mathbf{E}_{\text{inv}}$  and  $\mathbf{E}_{\text{dep}}$ . dPCA requires that a dimensionality of the model be specified explicitly, so we chose a dimensionality of 10 (5 for the stride-invariant and 5 for the stride-dependent subspace) based on findings of previous studies, but we also tested our results for dimensionality of 6 and 14

(split equally between the two subspaces), and did not find any significant changes in our results.

Additionally, we wanted to assess which aspects of the stride-dependent signals truly correspond to changes in neural activity because of the obstacle, and which aspects are just random fluctuations because of “noise.” To get an estimate of the noise distribution, we performed dPCA using just the first stride and the last stride. These strides occur before the obstacle begins to move, and two strides after the obstacle has been traversed, respectively, and are essentially the same as basic walking strides. Therefore, we do not expect any activity related to a volitional gait adjustment movement to be present in the neural activity, and thus any signals found in the stride-dependent subspace using only these strides would be just noise. We took these values to construct the null hypothesis distribution, and used a conservative cutoff value of the 99.99th percentile of this null distribution to determine which components of the signals in the full dPCA are significantly different from the basic walking or ongoing locomotion.

Finally, to quantify the timing of the changes in the stride-dependent subspaces in relation to the changes in the movement, we used the same analysis as before during the neural response characterization (see Fig. 5*k,l*). We calculated the cross-correlation between the mean Mahalanobis distance of the kinematics in the obstacle stride and the first component of the stride-dependent subspace in the obstacle stride at varying time lags.

**Principal angles.** To determine whether the subspaces we obtain from the dPCA are distinct, we calculated the principal angles between them, which measures the degree of orthogonality between two subspaces. Within each marginalization subspace, the dimensions are orthogonal (i.e., the rows within each encoder matrix form an orthonormal basis). However, because each marginalization projection is calculated independently, the resulting subspaces do not have to be orthogonal to each other, meaning that there could be a significant amount of overlap between the subspaces. To quantify the alignment between two subspaces, we calculated the principal angles between our stride-invariant and stride-dependent subspaces (Gallego et al., 2018).

The angles range from 0° to 90°, which indicates perfectly overlapping or perfectly orthogonal subspaces, respectively. To obtain the principal angles, we performed singular value decomposition on the product of the two encoder matrices, as follows:

$$\mathbf{E}_{\text{inv}}^T \mathbf{E}_{\text{dep}} = \mathbf{U} \Sigma \mathbf{V}. \quad (3)$$

The diagonals of the  $\Sigma$  matrix are the cosines of the principal angles, ordered from smallest to largest.

We performed dPCA on both the neural PETHs as well as the trial-averaged kinematics for the obstacle avoidance trials and calculated the principal angles between the stride-invariant and stride-dependent subspaces for both. Additionally, we also performed dPCA and found the principal angles on a simulated neural dataset that was constructed from the kinematics taken as a predictor, following the same model used by Gallego et al. (2018; see section Simulated neural control dataset below). To get a sense of the sampling variance, we performed 500 bootstrap resamples on the trials and calculated the principal angles for each bootstrap resample. (See Fig. 7*d,i* for the 95% confidence intervals of the bootstrap distribution.)

We hypothesized that the stride-invariant and stride-dependent subspaces are separate. To build a distribution of the principal angles under the null hypothesis, we used two subspaces that we know are completely aligned other than from intertrial variance: the  $\mathbf{E}_{\text{inv}}$  values (or  $\mathbf{E}_{\text{dep}}$  values) from two different bootstrap resamples. We performed two bootstrap resamples and calculated the principal angles between  $\mathbf{E}_{\text{inv, resample1}}$  and  $\mathbf{E}_{\text{inv, resample2}}$  as well as the angles between  $\mathbf{E}_{\text{dep, resample1}}$  and  $\mathbf{E}_{\text{dep, resample2}}$ . This was repeated 250 times to obtain our null distribution. (See Fig. 7*d,i* for the 97.5th percentile of the principal angles for this null distribution.)

**Rotational structure.** Locomotion is naturally cyclical, so we wished to determine whether our stride-invariant and stride-dependent subspaces exhibited rotational dynamics. To model rotational dynamics within the subspaces, we used jPCA, which is a specialized variant of a linear dynamical system (LDS; Churchland et al., 2012). jPCA is akin to a PCA analysis focused on rotational dynamics where the “rotational” aspect is indicated by

the imaginary number  $j$  in the acronym. The underlying assumption of dynamical systems models is that the current state of the latent dimensions is predictive of future states. LDS models the relationship between states as a linear difference equation with time-evolution matrix  $\mathbf{A}$ , as follows:

$$\mathbf{Y}_t = \mathbf{A} \mathbf{Y}_{t-1}. \quad (4)$$

Here,  $\mathbf{Y}_t$  is the low-dimensional neural activity in the stride-invariant or stride-dependent subspace at gait percentage  $t$ . In general-form LDS,  $\mathbf{A}$  can be obtained analytically through least-squares regression. In jPCA,  $\mathbf{A}$  is constrained to be skew symmetric, which results in a dynamical system that contains solely rotational components. While it is possible to solve for  $\mathbf{A}$  analytically in the constrained case, we followed the algorithm implemented in the study by Churchland et al. (2012), which uses a gradient-based optimization method. After obtaining  $\mathbf{A}$ , one can visualize the rotational dynamics by displaying the vector fields of the difference equation in the top two dimensions (see Fig. 7*e,j*). The jPCA algorithm was implemented with the MATLAB code provided by Churchland et al. (2012). Note that because we are already in a low-dimensional space, we did not perform the preprocessing step of using PCA to project into six dimensions before fitting for  $\mathbf{A}$ , as was done in the study by Churchland et al. (2012). To quantify the strength of rotational structure in each of the subspaces, we calculated the ratio of the jPCA fit  $R^2$  to an unconstrained LDS fit  $R^2$ . The unconstrained LDS can contain both rotational and nonrotational dynamics, but if the dynamics in the data are purely rotational, then the best unconstrained LDS  $\mathbf{A}$  would be the same as the jPCA  $\mathbf{A}$ , and the ratio would be 1. The more nonrotational dynamics that are present, the more deviant the jPCA fit will be from the best LDS fit and the lower the ratio. We calculated this metric for the stride-invariant data and the stride-dependent data for both neural and kinematic dPCA.

**Poisson linear dynamical system model.** dPCA explicitly attempts to extract dynamics related to the change in activity during the obstacle stride, and uses information about the stride type in the model. We also used the conditionally Poisson LDS (PLDS) model to extract single-trial dynamics, which are given no information about the stride type (Truccolo et al., 2005; Macke et al., 2011; Aghagholzadeh and Truccolo, 2016; Truccolo, 2016; Xing et al., 2019). This unsupervised dimensionality reduction method is a complementary approach to dPCA. Similar to PCA and dPCA, PLDS assumes that the recorded neural activity is the result of underlying neural modes. However, in PLDS the spiking of each neuron is modeled by a (conditionally) Poisson process rather than the usually assumed Gaussian distribution. Additionally, PLDS explicitly models temporal dynamics by incorporating a latent linear dynamical system (Gaussian process) similar to what was discussed in the previous section. The full model is described by the following:

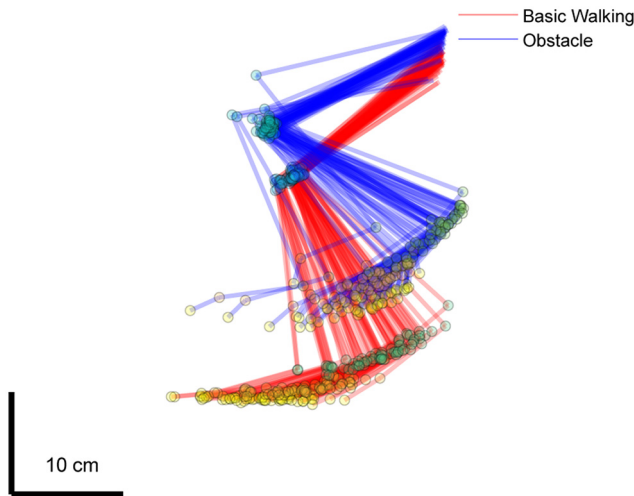
$$\begin{aligned} \mathbf{X}_{t+1} | \mathbf{X}_t &\sim \mathcal{N}(\mathbf{A} \mathbf{X}_t, \mathbf{Q}) \\ \mathbf{Y}_t &\sim \text{Poisson}(\lambda(t | \mathbf{X}_t)), \end{aligned} \quad (5)$$

where  $\mathbf{Y}_t$  is the vector of recorded spike counts of all neurons at time bin  $t$ ; it is distributed according to a conditionally multivariate Poisson process with (vector) intensity modeled as follows:

$$\lambda(t | \mathbf{X}_t) = \mathbb{E}[\mathbf{Y}_t | \mathbf{X}_t] = \exp(\mathbf{C} \mathbf{X}_t + \mathbf{d}),$$

where  $\mathbf{X}_t$  and  $\mathbf{X}_{t+1}$  are the vector of the activity of the neural modes at time bins  $t$  and  $t + 1$ , respectively;  $\mathbf{C}$  is the matrix of weights relating the neural modes to the conditional intensity function of the neurons, analogous to the  $\mathbf{B}$  in dPCA;  $\mathbf{d}$  is related to the baseline firing rate of the neurons;  $\mathbf{A}$  is the time evolution matrix governing the temporal dynamics of the neural modes, analogous to the  $\mathbf{A}$  matrix of the unconstrained LDS model in the previous section; and  $\mathbf{Q}$  is the covariance matrix of the additive Gaussian noise for the stochastic state evolution.

Unlike PCA and dPCA, there is no analytic solution for the model, so we used the expectation–maximization (EM) algorithm to infer the latent dimension activity and model parameters. Also, because of the nonlinearity, there is no closed-form solution to finding the posterior probability of the neural modes given the spiking activity observations



**Movie 1.** Stick figures illustrating the hindlimb kinematics across all trials for basic unobstructed walking (red) or the step over the obstacle (blue) in animal B. Video illustrates the kinematics before they were normalized to the gait cycle. Trials were time locked to the start of the swing phase (toe-off event). [View online]

and estimated parameters in the E-step, so we used the Laplace approximation, which formulates the posterior density at each time step as a Gaussian conditioned on the corresponding neural point process observations. We then estimate the values of the neural modes as the mean of this Gaussian which is calculated for each time point of each trial. A detailed description of the inference algorithm can be found in the studies by Aghagholzadeh and Truccolo (2014, 2016) and Macke et al. (2015). We initialize the EM iterations with (linear) subspace identification methods and ran the EM algorithm for a total of 60 iterations.

To estimate the dimensionality of the underlying neural subspace, we used the Akaike information criterion (AIC), as follows:

$$\text{AIC}(d) = 2(d^2 + d(d+1)/2 + nd) - 2\log(\mathcal{L}), \quad (6)$$

where  $d$  is the number of neural modes,  $n$  is the number of neurons, and  $\mathcal{L}$  is the likelihood function. The value that minimized the AIC was chosen as the final model dimensionality. Using this metric, we estimated the best-fit model dimensionality to be approximately nine.

**Simulated neural control dataset.** As an additional control, we additionally simulated a dataset of neural activity that was constructed from the kinematics taken as a predictor, following the same model used by Gallego et al. (2018). We simulated as many neurons as there were in our recorded dataset for each subject. The conditional intensity of neuron  $j$  was modeled as the weighted sum of the kinematics, as follows:

$$\lambda_j(t|\mathbf{Z}(t)) = \alpha_j + \sum_i \beta_{ij} \mathbf{Z}_i(t) + \epsilon_j(t), \quad (7)$$

where  $\mathbf{Z}_i(t)$  is the value of the normalized  $i$ th kinematic variable,  $\alpha_j$  is a baseline firing rate for the  $j$ th neuron and is uniformly sampled from [0, 10] spikes/s,  $\beta_{ij}$  is the weight of the  $i$ th kinematic variable onto the neuron, drawn from a Gaussian distribution of mean 0 and variance 1, and  $\epsilon$  is additive Gaussian noise with zero mean and a variance of 0.01. The kinematics consists of the 3D coordinates of the five joints and were normalized by subtracting the mean and scaling the amplitude to 1. The intensities were offset so that they were all positive. We then generated spike trains for each of the neurons and ran the dPCA principal angle and PLDS analysis on the simulated neural data.

**Spread metric.** Because PLDS is an unsupervised dimensionality reduction method, it may not necessarily extract subspaces which are invariant to the presence of the obstacle stride. Thus, we developed a spread metric to characterize the amount of overlap across all strides in the PLDS trajectories. The PLDS trajectories seen in Figure 8 were created by time normalizing the activity in the latent dimensions of each

trial to 0–100% of the gait cycle and then averaging across trials. We displayed the first three PLDS dimensions to visualize the time-varying activity of the neural modes throughout the six gait cycles as the animal stepped over the obstacle. Within this three-dimensional space, certain two-dimensional projections resulted in large amounts of overlap in the neural trajectories across the different strides. We used the MATLAB function *viewmtx()* to calculate the projections at various azimuth and elevation viewing angles. We then chose the projection that contained the most overlap as our stride-invariant subspace. A different viewing angle that highlights the changes in the neural trajectories was chosen by visual inspection as the stride-dependent subspace.

To quantify the amount of overlap in the low-dimensional PLDS projections between different strides, we created a spread metric that determines how deviant the neural trajectories become relative to a reference baseline stride. Because we expect the obstacle stride to have the greatest deviation from the other strides, we chose that stride as the baseline.

Let the vector  $\mathbf{a}_{\text{ref},t}$  be the coordinates of the reference stride in the projected 2D space at gait percentage  $t$ . For each of the other strides  $i = 1 \dots 5$ , we calculated the Euclidean distance of the closest point to  $\mathbf{a}_{\text{ref},t}$  within 10 gait percentages, as follows:

$$D_{i,t} = \min_{-10 \leq k \leq 10} \|\mathbf{a}_{\text{ref},t} - \mathbf{a}_{i,t+k}\|^2. \quad (8)$$

We chose to use all points within 10 gait percentages to account for any “slippage” because of imperfect time normalization between the strides. We then took the maximum distance across all of the strides,  $\max D_{i,t}$  to find the spread metric at gait percentage  $t$ . Finally, we obtained the final spread metric by taking the 90th percentile across gait percentages  $20 \leq t \leq 80$ . We excluded the first and last 20 gait percentages to avoid artifacts from edge effects and used the 90th percentile to exclude outliers.

**Computation of explained variance.** For PCA and dPCA, we measured how much neural variance in the PETHs the low-dimensional neural modes were able to explain by calculating the VAF:

$$\text{VAF} = \frac{\|\mathbf{Y}\|^2 - \|\mathbf{Y} - \mathbf{C}\mathbf{B}\mathbf{Y}\|^2}{\|\mathbf{Y}\|^2}, \quad (9)$$

where  $\mathbf{Y}$  denotes here the matrix of PETHs of all neurons,  $\mathbf{B}$  is the decoder matrix (Eq. 1);  $\mathbf{C}$  is the “encoder” matrix, which for PCA and dPCA corresponds to the matrix that maps the latent dimensions back up to the high-dimensional neural space. The indicated norm is the Frobenius norm.

**Neural decoding.** We used a Wiener filter decoder of order 10 to predict single-trial kinematics at each gait percentage time point  $t$ , denoted by  $\hat{\mathbf{Z}}_t$ , using various neural inputs  $\mathbf{Y}_t$ , as follows:

$$\hat{\mathbf{Z}}_t = \sum_{\tau=0}^9 \mathbf{H}_\tau \mathbf{Y}_{t-\tau}. \quad (10)$$

Here,  $\mathbf{Y}_{t-\tau}$  denotes the single-trial vector of firing rates (one component per neuron) time shifted by  $\tau$  gait percentages, and  $\mathbf{H}_\tau$  is the matrix of decoding weights, which we computed through least-squares regression on training data. For all of our decoding analyses, we used the toe height as the decoded kinematic variable.

We tested whether a decoder trained to predict kinematics during basic locomotion could generalize to obstacle avoidance movements. We used the firing rates of the full neural population as the input vector  $\mathbf{Y}_t$ , and calibrated the decoder weights using the neural data and kinematics from the stride three strides before the obstacle stride (stride −3). We then used those weights to predict the kinematics during the subsequent strides, including the obstacle stride. We also tested the opposite (i.e., whether a decoder trained on the obstacle avoidance stride could decode kinematics during basic locomotion). In this case, the weights were trained on the neural and kinematic data during the obstacle stride and applied to each of the other strides. Note that for testing decoder



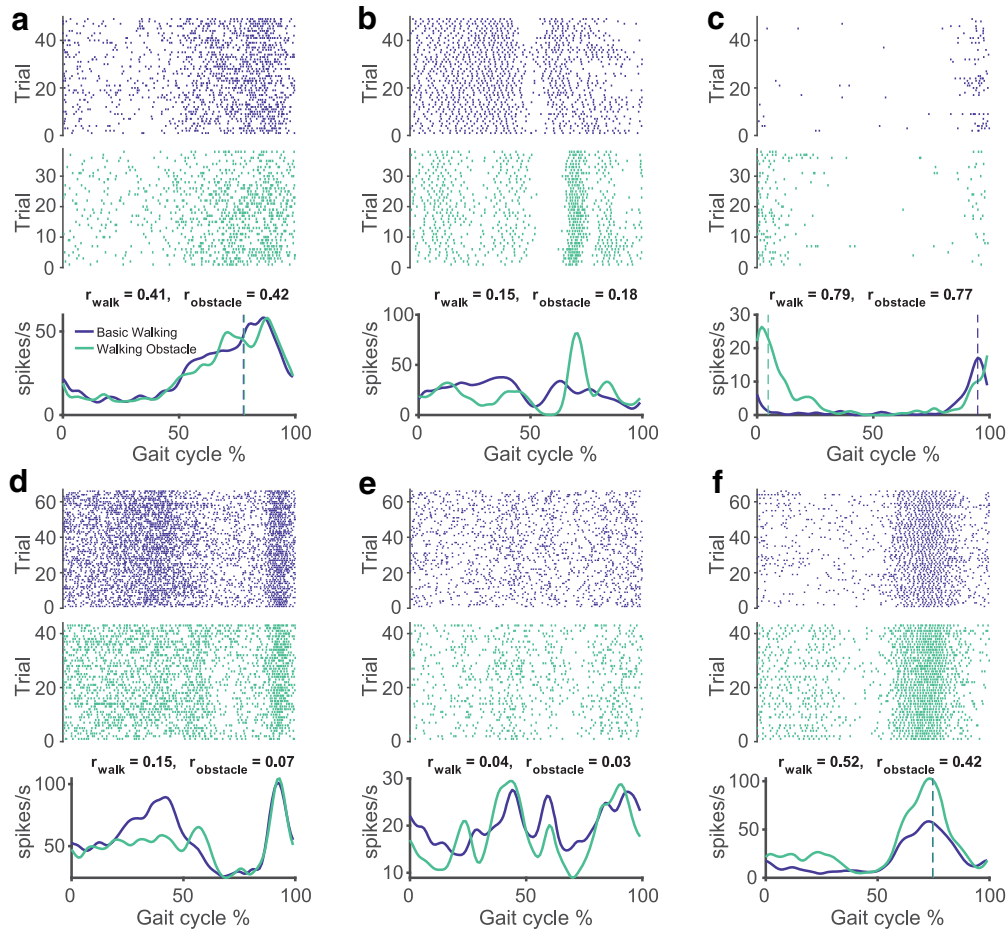


**Figure 4.** Example M1 neurons during basic walking and obstacle stepping. Example raster plots and PETHs from the activity of leg-M1 neurons. Top raster plot is for basic walking trials, while bottom raster plot is for obstacle-stepping trials.  $r$  Values represent the dispersion of the neural activity around the gait cycle, and the dotted lines represent the preferred phases of the firing activity of the neuron, for neurons with strongly modulated, unimodal activity. **a–c**, Activity of neurons from animal B. **d–f**, Activity of neurons from animal S.

generalization, we did not need to use cross-validation since the training set for the decoder was completely separate from the testing set. However, we also measured how well the decoders trained on either the basic walking or the obstacle stride could decode the kinematics during that same stride. In these cases, we used leave-one-out cross-validation by removing one trial from the training set and using it as the testing set. As a control, we built a decoder trained on all of the strides and calculated the decoding performance across all of the strides using leave-one-out cross-validation as well.

When testing decoder performance using low-dimensional neural modes as inputs, we used the same procedure, but instead of using the single-trial neural firing rates  $\mathbf{Y}_t$  as inputs in Equation 10, we used the low-dimensional neural trajectories obtained with dPCA. We measured the decoding performance using just the latent dimensions within the stride-invariant subspace or the dimensions in both the stride-invariant and stride-dependent subspace. In both cases, all of the strides were included in the training set and leave-one-out cross-validation was used.

We measured decoder performance by calculating the mean squared error between the decoded kinematics  $\hat{\mathbf{Z}}_t$  and the true kinematics across all gait percentages, as follows:

$$\text{MSE} = \frac{\sum_{t=1}^{100} (\mathbf{Z}_t - \hat{\mathbf{Z}}_t)^2}{100}. \quad (11)$$

**Data availability.** The data that support the findings of this study are available from the corresponding author upon reasonable request. Peer-reviewed, published libraries for dPCA, jPCA, and circular statistics are

referenced in the text at appropriate locations. The analysis code that supports the findings of this study can be found at <https://github.com/neuromotion/Distinct-neural-subspaces-during-obstacle-avoidance>.

## Results

### Animals conducted volitional gait adjustments in an obstacle avoidance paradigm

Animals were successfully trained to enter the Plexiglas enclosure on top of the motorized treadmill and continuously walked at 2.2 km/h. Within the enclosure, an actuated Styrofoam bar moved toward the animal at 2.2 km/h, giving the perception of an obstacle approaching along the treadmill belt (Fig. 2a). Both animals successfully raise their limbs to step over the obstacle without hitting it while maintaining their ongoing walking movements. A go tone would alert the animal of the oncoming obstacle, and the operator would manually time the start of the obstacle movement to a particular gait event (e.g., the instant the right hand made contact with the floor) to maintain consistency in the avoidance movement across trials. Although there was some amount of jitter in the timing of the obstacle initiation relative to the gait cycle, the variance was rather small (SD: 2.7% of the gait cycle for animal B; and 2.8% of the gait cycle for animal S). Each trial consisted of one obstacle run, which included the stride where the leg was lifted over the obstacle (denoted as stride 0), three strides before the obstacle stride (strides −3 to −1), and two strides after the obstacle stride (Fig. 2c,



strides 1–2). Additionally, we collected data from the animals as they continuously walked on the treadmill without any obstacle movement, which we will refer to as basic walking. Example neural activity and kinematics of an obstacle stepping trial, along with the gait pattern and obstacle position are shown in Figure 2c.

We recorded 38 obstacle avoidance trials from animal B and 43 trials from animal S, along with 49 basic walking trials from animal B and 66 trials from animal S, from a recording session from each animal. The recordings were conducted 44 d after the array implantation in animal B and 55 d after the implantation for animal S. The average duty cycles for the strides were 67% for animal B and 69% for animal S. The average stride durations were 1126 ms for animal B and 1119 ms for animal S. In general, the durations of the gait cycle were consistent across trials, with the SD being 44 ms for animal B and 65 ms for animal S.

### General movement strategy is preserved during obstacle avoidance while the step height is increased

The limb movement throughout all the strides, including the obstacle stride, follows the same stepping pattern. Horizontal and vertical positions of the joints increased and decreased at similar phases of the gait cycle, while the main difference between the obstacle stride and the other strides is in the magnitude of the movements. Both animals had to raise their hindlimbs considerably higher than during their normal walking gait to clear the obstacle (Fig. 2d,e,g,h, Movie 1;  $p < 10^{-5}$ , Wilcoxon rank-sum test). During basic walking, the average stride height was 3.66 cm for animal B and 4.45 cm for animal S, and increased to 17.95 and 11.28 cm for the obstacle stride, respectively. However, the stride durations were similar for all the strides, with the exception of the stride immediately before the obstacle stride in animal B, which was shorter than usual (Fig. 2f,i;  $p < 10^{-5}$ , Wilcoxon rank-sum test). We refer to the first hindlimb to step over the obstacle as the leading limb and the second hindlimb as the trailing limb. In both animals, the right limb was the trailing limb over the obstacle.

The obstacle did not start moving until two strides before (–2) the obstacle stride in animal B and one stride before (–1) the obstacle stride in animal S, meaning that from the perspective of the animal, the first gait cycle in the obstacle avoidance trials should be essentially the same as the gait cycle during basic walking. Indeed, the stride height and duration are virtually identical between these two strides (Fig. 2e,f,g,h). Between the next two strides, the animals could see and were aware of the obstacle moving toward them, although the stride height remained unchanged for these strides.

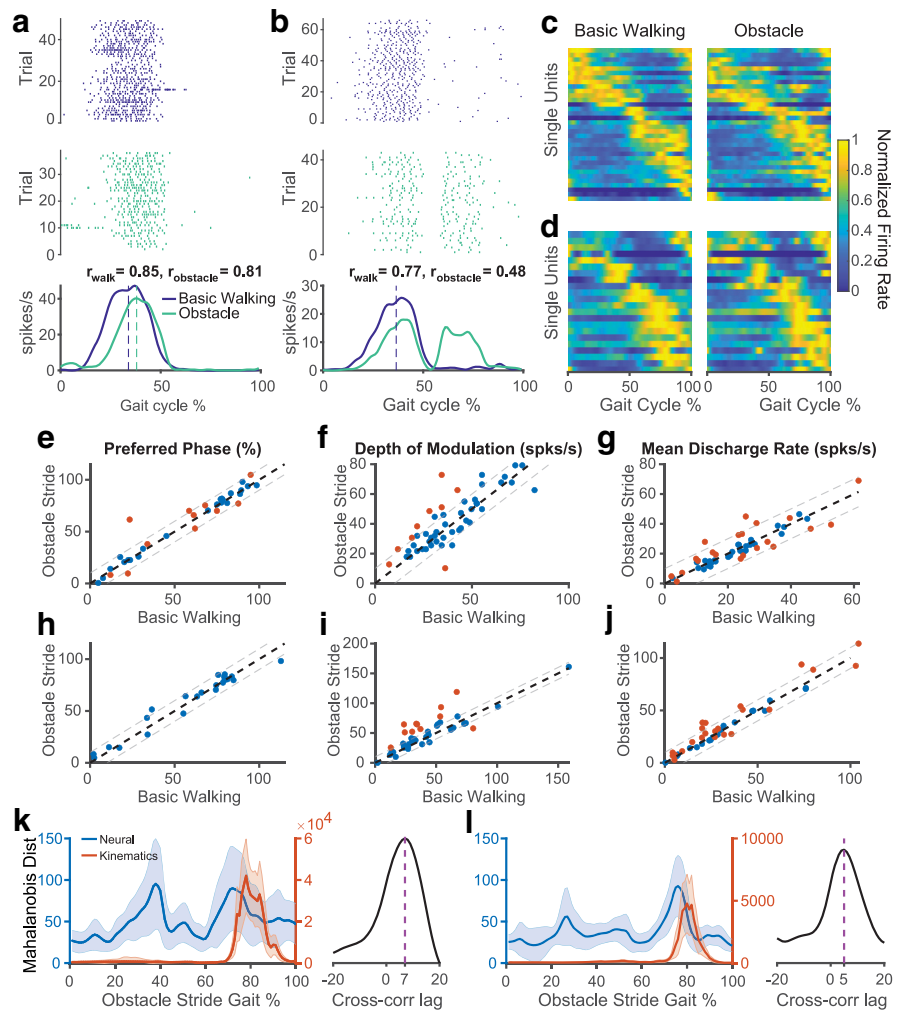


**Figure 5.** The activity of most M1 neurons are phasically tuned to the gait cycle and increase their depth of modulation during obstacle stepping. **a**, Example plot of activity of a neuron from animal B demonstrating a small shift in preferred phase in response to obstacle stepping. **b**, Same as in **a** but for an example neuron from animal S demonstrating complex changes in activity. **c**, Activity of all phasically modulated neurons for animal B during both basic walking (left) and the stride stepping over the obstacle (right). Neurons are sorted by preferred phase during basic walking, with the earliest firing neurons on top. Neuron ordering is kept the same for both basic walking and obstacle-stepping plots. The activity of each neuron is normalized to its maximum firing rate. **d**, Same as in **c**, but for animal S. **e–g**, Changes in preferred phase, depth of modulation, and average firing rate, respectively, of the neural population between the basic walking stride and the obstacle stride. Each point represents an individual neuron, orange indicates statistically significant change [permutation test with 1000 label reshuffles, with false discovery rate (FDR) correction for multiple comparisons; FDR set to 5%]. Thick dotted line indicates no change, thin dotted lines delineate a change of 10% for preferred phase and 10 spikes/s for depth of modulation and average firing rate. **h–j**, Same as in **e–g** but for animal S. **k**, Mahalanobis distance between the stride over the obstacle and the stride before any obstacle movement for the population of neural firing rates (blue) or the kinematic variables (orange). Right plot shows the cross-correlation between the neural and kinematic distances across multiple gait percentage lags with the dotted line indicating the peak lag. Positive indicates neural leading kinematics. **l**, Same as in **k** but for animal S.

After clearing the obstacle, the stride height returns to normal pre-obstacle ranges. In summary, despite the large change in kinematics in the obstacle stride, the subjects returned to normal walking quickly after avoiding the obstacle, and, with the exception of animal B taking a smaller and quicker stride right before the obstacle stride, they did not drastically alter their gait leading up to the obstacle stride. Additionally, we observed a change in the interlimb coordination among all four limbs from stride –1 to stride 2.

### M1 neurons show increased activity but little phasic reorganization during obstacle avoidance

We then characterized the response properties of individual neurons in leg area of M1. We recorded 50 neurons from animal B

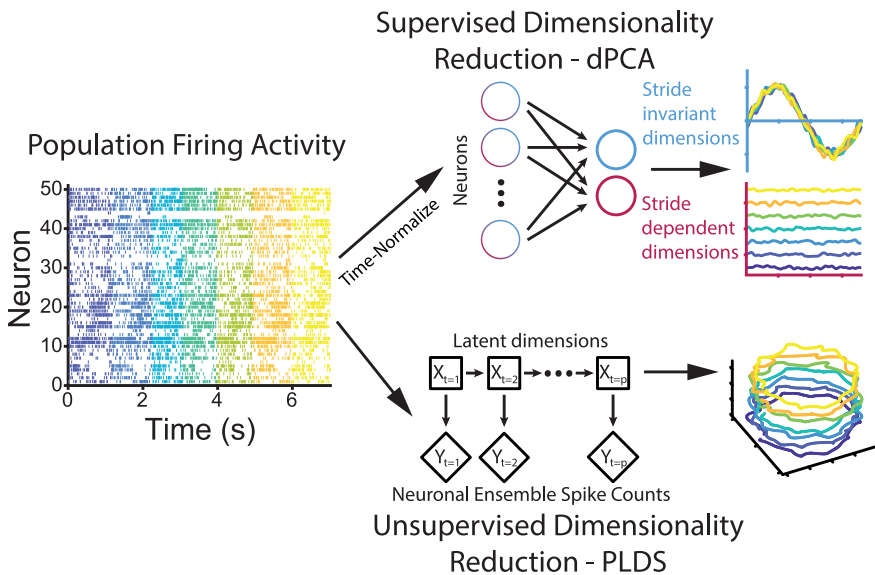


**Figure 6.** Analysis of low-dimensional motor cortical dynamics. Diagram illustrating the general analysis pipeline. Two complementary approaches were used: a supervised approach, dPCA, where the type of the stride (obstacle vs nonobstacle) was explicitly used by the model (top); and an unsupervised approach, PLDS, where the model was agnostic to the type of stride (bottom). A time bin of 10 ms was used for both dPCA and PLDS. In addition, for dPCA time was normalized with respect to the gait cycle. See Materials and Methods for details on the dPCA and PLDS models and analyses.

and 42 neurons from animal S. Figures 4 and 5*a,b*, illustrate the activity of example neurons during both basic walking (purple) and the stride over the obstacle (teal). To compare the activity across trials, which had some slight variations in duration, the spike trains were time normalized to 0–100% of the gait cycle (Materials and Methods; Fig. 3*c*). Consistent with previous M1 recordings during locomotion, the majority of neurons tended to increase their firing rate during specific phases of the gait cycle (Foster et al., 2014; Yin et al., 2014; Xing et al., 2019). Although many of these neurons fired at around a single phase of the gait cycle (Figs. 4*c*, 5*a*), we also found neurons that had multimodal PETHs (Fig. 4*d*). We used circular statistics (Drew and Doucet, 1991; Berens, 2009) on the unimodal PETHs to determine the preferred phase and dispersion ( $r$ ) of the discharge rate of the neurons around the gait cycle (Fig. 3*e*). We applied the Rayleigh test to identify neurons whose discharge rates were not significantly modulated to the gait cycle and further classified unimodal, modulated neurons as weakly modulated if they had an  $r$  value  $<0.15$  during basic walking. Figure 3*f* shows the distribution of dispersion values and indicates that the discharge rates of most of our recorded neurons are strongly modulated. Since the preferred phase is only well defined for the discharge rates of neurons that are both significantly modulated to the gait cycle and have a unimodal PETH, we excluded neurons that are multimodal or whose discharge rates are weakly modulated from preferred phase calculations (but not depth of modulation or mean firing rate calculations).

We found that for both animals, the preferred phases of the population of recorded neurons spanned the whole gait cycle (Fig. 5*c,d*), consistent with previous studies in felines and macaques (Beloozerova and Sirota, 1998; Drew et al., 2008; Foster et al., 2014; Yin et al., 2014; Xing et al., 2019). Additionally, neurons tend to fire at similar phases during the obstacle avoidance step as during basic walking (Fig. 5*c–e,h*). Only 4 of 34 (animal B) and 2 of 22 (animal S) of the strongly modulated neurons had shifts in preferred phase  $>10\%$  of the gait cycle. However, most neurons tended to increase their depth of modulation during the

obstacle step (average increase: for animal B, 6.37 spikes/s; for animal S, 11.62 spikes/s), reflecting the larger amplitude of the movement (Fig. 5*f,i*). The mean firing rates also saw an overall increase, although the change is not as large (average increase: for animal B, 0.52 spikes/s; for animal S, 2.25 spikes/s; Fig. 5*g,j*), although we note that this analysis favored active neurons, and small changes in firing rate may be significant for neurons whose baseline activity was already low. The increase in depth of modulation could potentially reflect larger muscle activation requirements for lifting the leg higher or increased requirements for accuracy (Beloozerova and Sirota, 1993*a*). Finally, we note that many of the neurons exhibited complex changes in firing activity beyond simple phase shifts or changes depth of modulation (Fig. 4*b,d*).

Lifting the leg over the obstacle involves a decision to move the limbs in a specific way, which requires descending input from motor cortex. We therefore hypothesized that there would be a change in neural activity preceding the modifying movement to the gait. We determined

when the changes in the obstacle avoidance stride occurred by calculating the Mahalanobis distance between stride 0 (the obstacle stride) and stride  $-3$  (the stride before any movement in the obstacle) at each percentage of the gait phase. Unsurprisingly, we saw a large increase in the difference between the kinematics during the swing phase (Fig. 5*k,l*, orange plot;  $p < 10^{-5}$ , Wilcoxon rank-sum test), corresponding to the increase in step height. We also observed an increase in the difference of the neural population immediately before the kinematic divergence (Fig. 5*k,l*, blue plot;  $p < 10^{-5}$ , Wilcoxon rank-sum test), giving evidence for the presence of an efferent signal in M1 related to the action of lifting the leg over the obstacle. Cross-correlation analysis determined that the neural modulation preceded the change in kinematics by 7% of the gait cycle in animal B and 5% in animal S, which, using the average stride durations, corresponds to 72.1 and 52.3 ms, respectively. One possible explanation, although unlikely, for this signal could be that cortex engages separate subpopulations for maintaining locomotion and for carrying out voluntary gait adjustment, and would only recruit the neurons related to voluntary movement during the obstacle stride. However, within the population we are recording from, we did not see the emergence of any clusters in the top left in our depth of modulation plots, indicating the lack of obstacle avoidance-specific neurons (Fig. 5*f,i*). We also observed a deviation in neural activity earlier in the stride,  $\sim 20$ –40% of the gait cycle. This change could reflect preparatory activity as the animals are observing the approaching obstacle and formulating the motor plan to step over it.

Together, these results indicate that M1 neurons are active during basic locomotion and that the same population is also predictive of volitional gait-adjusting movements. Previous work in rodents has shown that M1 population activity, although present during both basic treadmill walking and stationary voluntary movements, resides in separate subspaces across the two behaviors (Miri et al., 2017). We wanted to determine whether this

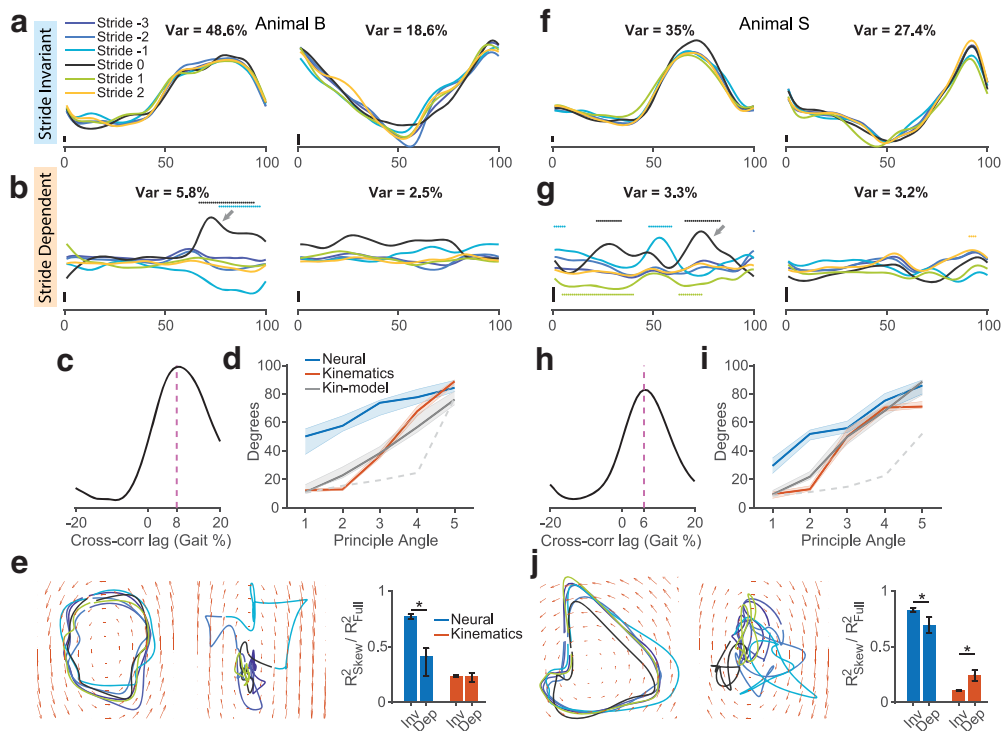


**Figure 7.** dPCA separates neural activity into obstacle stride-invariant and stride-dependent subspaces. **a, b, f, g**, Top two stride-invariant (**a, f**) and stride-dependent (**b, g**) demixed components. Each of the strides surrounding the obstacle stride (stride 0) are plotted individually. Numbers at the top represent percentages of the total variance for each component. Arrows indicate the increase in the stride-dependent neural modes during the obstacle stride that account for the peaks in **c** and **h**. Colored dots/lines indicate points where the stride-dependent components were significantly greater than noise (see Materials and Methods). **c, h**, Cross-correlation between the change in kinematics and the change in activity within the stride-dependent subspace across multiple gait lags, similar to Figure 5, **k** and **l**. **d, i**, Principal angles between the stride-invariant subspace and stride-dependent subspace for both neural dPCA and kinematics dPCA. Error bars represent 95% confidence intervals for 500 bootstrap resamples. Dotted gray line represents the 97.5th percentile of the null distribution of completely overlapping subspaces. **e, j**, First two stride-invariant components (left plot) or stride-dependent components (middle plot) are plotted against each other to visualize rotational structure (or lack thereof). The slope fields for the rotations inferred with jPCA are shown as orange arrows. Right plot, Ratio of the jPCA model  $R^2$  to an unconstrained LDS model  $R^2$  to quantify the strength of rotations. For dPCA used on neural activity, error bars are 95% confidence intervals for 500 bootstrap resamples. Stars indicate statistically significant difference (Wilcoxon rank-sum test,  $\alpha = 0.05$ ). Var, Variance; Kin, kinematics; corr, correlation; Inv, invariant; Dep, dependent.

compartmentalization of neural activity is maintained when both types of movements have to be conducted simultaneously such as in obstacle avoidance. We therefore used dimensionality reduction techniques to investigate whether M1 used specific neural subspaces for carrying out the gait adjustment, and whether these subspaces are distinct from the ones present during basic locomotion (Fig. 1*b*).

### dPCA reveals division of neural modes into obstacle-related and obstacle-invariant subspaces

dPCA is a statistical method that decomposes neural activity into subspaces associated with specific task parameters (Fig. 6). The neural modes that comprise the subspaces are computed through linear combination of the activity of each neuron. The weights of this linear combination are optimized to find projections that are either invariant or dependent on specific task parameters. Here, we used dPCA to extract subspaces that were agnostic to the gait adjustment (stride invariant) and also subspaces that captured the change in population activity during the gait adjustment (stride dependent). We found that 10 dPCA components were able to explain 87.2% and 88.4% of the variance for animal B and animal S, respectively.

The stride-invariant subspace accounted for most of the neural variance (77.1% for animal B, 80.7% for animal S) and, indeed, showed very little modulation across strides (Fig. 7*a,e*), preserving the same time-varying activity throughout all the strides during obstacle stepping. The stride-dependent activity

accounted for 11.9% of the variance in animal B and 11.0% for animal S. We observed large deviations in the stride-dependent components during the stride immediately before and the stride over the obstacle (Fig. 7*b,f*;  $p < 0.0001$ ; see Materials and Methods), suggesting that these components capture an increase in M1 engagement during those strides. Additionally, we compared the timing of these shifts in relation to the changes in the kinematics during the swing phase and found that, like with the population firing rates, the activity of the stride-dependent components preceded the gait changes (Fig. 7*c,h*).

Although dPCA was able to find subspaces that are invariant and subspaces that are dependent on the gait modification, the nature of the algorithm does not guarantee that the stride-invariant and stride-dependent subspaces are orthogonal. For example, we were also able to find stride-invariant and stride-dependent subspaces for the kinematics, yet these subspaces could be largely overlapping. Principal angles have been used in previous studies to determine the alignment between two subspaces (Gallego et al., 2018). To demonstrate that any results regarding the neural subspaces are not simply trivially reflecting the properties of the kinematics of the movement, we also performed control analyses on the kinematics themselves along with a neural dataset simulated from the kinematics similar to what was conducted in the study by Gallego et al. (2018). We calculated the principal angles between the stride-invariant and stride-dependent neural subspaces, and found that they were greater than the principal angles between the kinematics subspaces and kinematic-



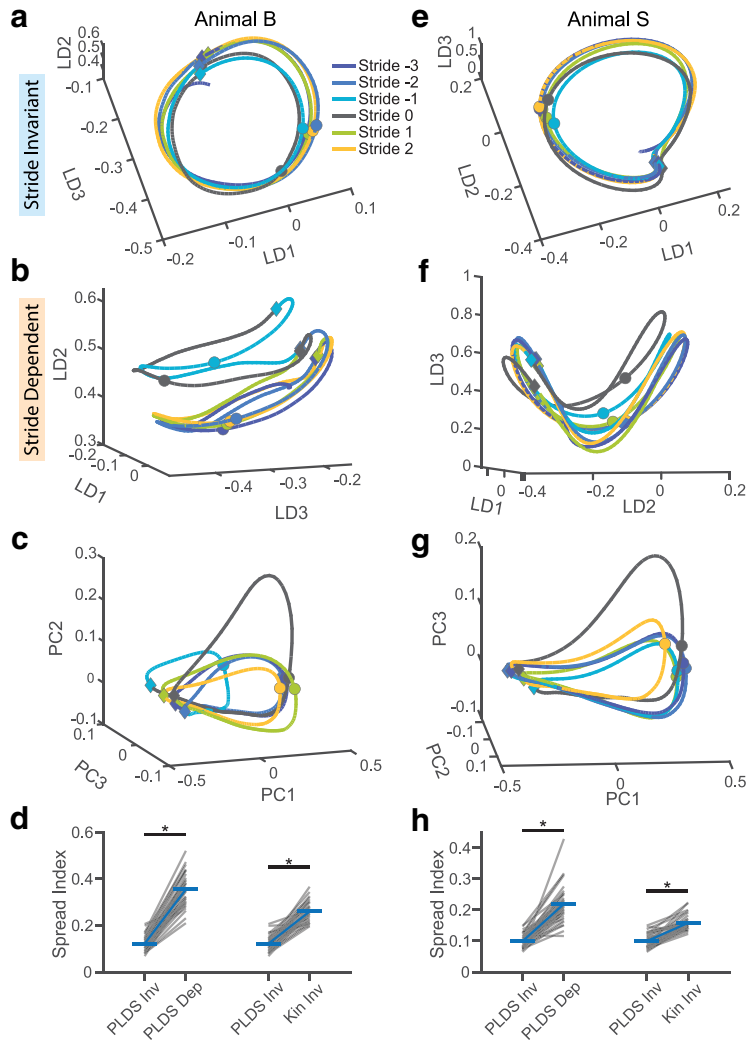


**Figure 8.** PLDS also extracts neural modes invariant to obstacle stepping. **a, e**, Neural trajectories from three neural modes, or latent dimensions (LDs), inferred from the PLDS model. Each of the strides surrounding the stride over the obstacle (stride 0) are plotted individually. The view angle of the trajectories is chosen to maximize the overlap between all of the strides according to a spread index (see Materials and Methods). The projection into this view represents the stride-invariant subspace. Circular dots indicate the transition from the stance phase to the swing phase in each stride, while diamond dots indicate the transition from the swing phase to the stance phase of the next stride. **b, f**, Same plot as in **a** and **e** but with a view angle that highlights the differences across strides, representing a stride-dependent subspace. **c, g**, Top three PCA components of the kinematics for the same strides as the PLDS plots. **d, h**, Spread index quantifying how much the trajectories overlap or diverge across strides (see Materials and Methods). We compared the amount of divergence between the trajectories in the stride-invariant neural subspaces with the stride-dependent neural subspaces (left) as well as the stride-invariant neural subspaces with the stride-invariant kinematic subspaces (right). Stars indicate statistical significance (Wilcoxon signed-rank test,  $\alpha = 0.05$ ). **a–d**, Animal B; **e–h**, animal S. Inv, invariant; Dep, dependent.

simulated subspaces (Fig. 7*d,i*; Materials and Methods) as well as a bootstrapped null distribution (Materials and Methods;  $p < 0.05$  significance level).

It is also possible that these dPCA components reflect the activity of specific subpopulations of neurons, rather than the whole population. We investigated this possibility by examining the projection weights of each neuron (Kobak et al., 2016; Gallego et al., 2018). We found that the distribution of the weights for all of the components is unimodal, with small weights for most neurons and no outliers. Additionally, we performed cluster analysis on the neural weights (Rodriguez and Laio, 2014; Kobak et al., 2016) and found that the neurons formed only a single cluster, indicating that the dPCA components are distributed across the whole neural population rather than corresponding to specific subpopulations.

Finally, we hypothesized that since the cyclic locomotor rhythm was a common factor across all of the strides, the stride-invariant subspace would contain significant rotational dynamics, while the dynamics of the stride-dependent subspace, which represents the precisely timed motor adjustments on the gait, would be less rotational. We used jPCA to fit a rotational dynamical system to both sets of subspaces, and quantified the rotational strength as the ratio of the coefficient of determination ( $R^2$ ) of the jPCA model to the  $R^2$  of an unconstrained dynamical systems model (Churchland et al., 2012). Figure 7, *e* and *j*, illustrates the fitted rotational dynamics of the first two latent dimensions in both subspaces. In agreement with our hypothesis, we found that there was significantly more rotational structure in the stride-invariant than the stride-dependent subspace (permutation test,  $p = 0.002$  for both animals;  $n = 500$  permutation shuffles for all dPCA statistical tests). In contrast, when we tested the kinematics, we found that the stride-invariant and stride-dependent subspaces were both less rotational. Finally, although we chose to use a dimensionality of 10 in our dPCA model (5 dimensions for stride-invariant subspaces, 5 for stride-dependent subspaces) based on previous dimensionality reduction studies (Yu et al., 2009; Sadtler et al., 2014; Vargas-Irwin et al., 2015; Xing et al., 2019), we tested these findings across a range of dimensionalities and obtained similar results.

### Unsupervised dimensionality reduction shows similar separation of neural subspaces

dPCA is a powerful technique that uses labeled data to extract task-related subspaces. To ensure that our findings are not simply the result of the partially supervised nature of dPCA, we also used an unsupervised dimensionality reduction model completely agnostic to the stride type (Fig. 6). One such model, PLDSs, explicitly infers the low-dimensional dynamics through a time-evolution matrix, resulting in smooth single-trial neural trajectories without the need for trial

averaging (Fig. 8*a,b,e,f*; Macke et al., 2011; Aghagholzadeh and Truccolo, 2014; Xing et al., 2019). We have previously shown that the PLDS neural modes were able to reconstruct limb kinematics just as well as the full population rates and better than PCA components during locomotion (Xing et al., 2019).

The top three dimensions accounts for most of the variance (for animal B, 60.8%; for animal S, 86.4%). The neural trajectories in these components for each of the strides are shown in Figure 8, *a* and *b*, for animal B, and in Figure 8, *e* and *f*, for animal S. Interestingly, there are projections of this space where the neural trajectories completely overlap, regardless of the stride (Fig. 8*a, e*), while other projections reveal a divergence of the trajectories during the obstacle stride (Fig. 8*b,f*). We defined the stride-invariant subspace as the projection that results in the greatest amount

of overlap across all of the strides. We quantified the amount of overlap using a spread metric (Materials and Methods) and optimized for the projection that minimized this spread metric. There are two notable features in these projections that are consistent in both animals. First is the clear rotational structure in this subspace, corroborating our results from the dPCA. Second is the large amount of invariance between the trajectories across the different strides, despite the large change in movement during the obstacle stride. We emphasize that, unlike dPCA, the PLDS model is not designed to specifically identify neural modes invariant to any particular variable, so it is entirely possible that the modulation in response to the voluntary gait adjustment pervades all the top PLDS neural modes (Fig. 1c). Indeed, the top three principal components of the kinematics demonstrate this case, as there are no projections resulting in the same amount of overlap between the obstacle stride and the basic walking strides (Fig. 8c,g). When comparing the smallest achievable spread index for the kinematics and the PLDS trajectories, the kinematics was significantly larger (one-tailed Wilcoxon signed-rank test:  $n = 38$  trials,  $p = 4.03 \times 10^{-8}$  for animal B;  $n = 43$  trials,  $p = 6.23 \times 10^{-9}$  for animal S) by  $\sim 2.13$  times for animal B and 1.58 times for animal S (Fig. 8d,h). As an additional control, we simulated a neural dataset using only kinematics data, following the method of Gallego et al. (2018). Like with the kinematics PCA, there is no projection in which the ongoing activity is unaffected by the obstacle movement (Fig. 9).

Projecting the PLDS trajectories along a different angle reveals the modulation of the latent activity in response to the voluntary intervention (Fig. 8b,f) and the significantly greater spread index compared with the stride-invariant projection (for animal B,  $p = 4.03 \times 10^{-8}$ ; for animal S,  $p = 6.23 \times 10^{-9}$ ). Like in dPCA, the trajectories appear to diverge away from the basic walking activity (Fig. 8b,f, purple and dark blue traces) during the obstacle stride and the preceding stride (Fig. 8b,f, light blue and black traces), before returning to the preobstacle region (Fig. 8b,f, green and orange traces). These results indicate that a consistent set of rotating neural modes throughout the whole obstacle-stepping sequence is maintained in the cortical activity, while a separate set of modes encode the actual gait adjustment movements. The time evolution of the neural activity in the PLDS latent dimensions as the animal steps over the obstacle is illustrated in Movie 2.

### Decoding of movement kinematics does not generalize between basic locomotion and obstacle stepping

The existence of neural modes correlating with the efferent intervention of M1 onto the locomotor movements suggests that any kinematic decoders trained on neural data during basic locomotion (and therefore not requiring any gait intervention) would not capture the information represented in these modes. Therefore, we hypothesized that decoders would not be able to generalize across strides during obstacle stepping. To test

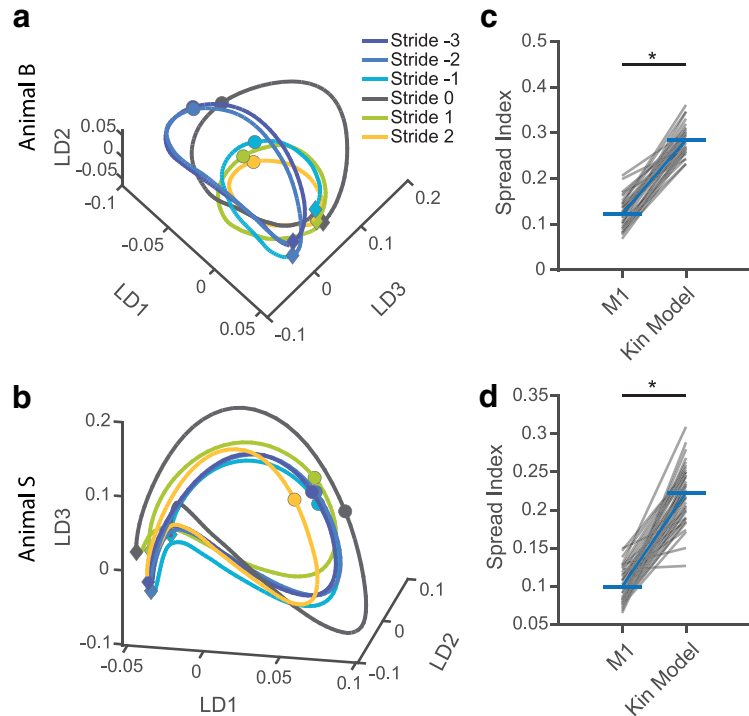
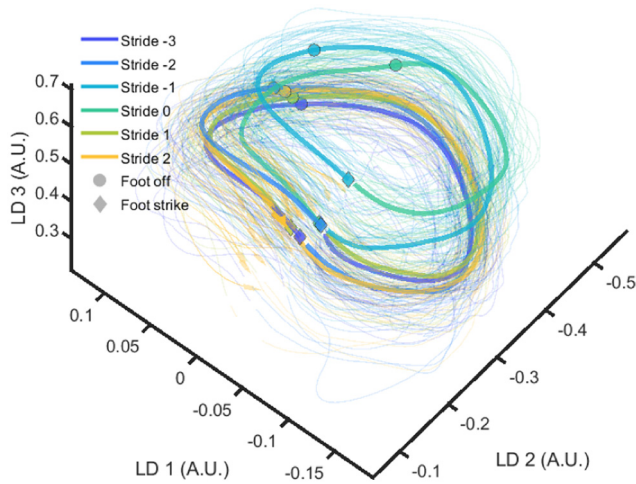


**Figure 9.** PLDS with model neural data derived from kinematics. For both animal B and animal S, we simulated neural activity using the kinematics and applied our PLDS analysis (see Materials and Methods). **a, b**, The neural trajectories in the first three latent dimensions. There is no projection that results in the same level of overlap across all the strides as in the M1 neural trajectories. **c, d**, The minimum attainable spread metric for either the real M1 neural data or the kinematic-modeled neural data.

this hypothesis, we used a Wiener filter decoder to predict the toe height, the most pertinent kinematic variable for clearing the obstacle, from the neural activity. We trained the decoders with neural and kinematic data from only stride  $-3$  (walk trained) or only stride  $0$  (obstacle trained) and measured the decoding performance throughout all the strides. We found that while the walk-trained decoder was able to reconstruct the kinematics fairly accurately for the strides before and after the obstacle stride, there was a large amount of error when decoding the swing phase of the obstacle stride (Fig. 10a,b, blue). Similarly, the obstacle-trained decoder was able to accurately decode the toe height during the obstacle stride, but was unable to do so with the surrounding strides (Fig. 10a,b, purple).

Finally, to directly test the necessity of the stride-dependent neural modes for capturing the change in kinematics during the obstacle stride, we trained a decoder on neural modes from just the stride-invariant subspace of dPCA, as well as a decoder trained on all neural modes, including those from the stride-dependent subspace. We trained the decoder using the activity from all the strides and performed leave-one-out cross-validation. We found that while the decoder trained on just the stride-invariant neural modes performed well on the strides before and after the obstacle stride, it performed poorly on the obstacle stride itself, despite having been trained on data during the obstacle stride. When we included the stride-dependent modes, there was no effect on the first stride (for animal B,  $p = 0.1108$ ; for animal S,  $p = 0.3878$ ; Wilcoxon rank-sum test), but increased the decoding performance during the obstacle stride (Fig. 10c,d;  $p < 10^{-5}$ , Wilcoxon rank-sum test), suggesting that much of the movement information involved in the gait adjustment is contained in these neural modes.



**Movie 2.** PLDS neural trajectories during obstacle avoidance. This movie illustrates the time-varying neural activity in the first three PLDS latent dimensions (LDs) of animal B. The obstacle stride, three strides before the obstacle stride and two strides after the obstacle strides, are shown. Thin traces represent the activity for each individual trial. Thick traces represent the trial-averaged activity (e.g., what is displayed in Fig. 8*a,b*). [View online]

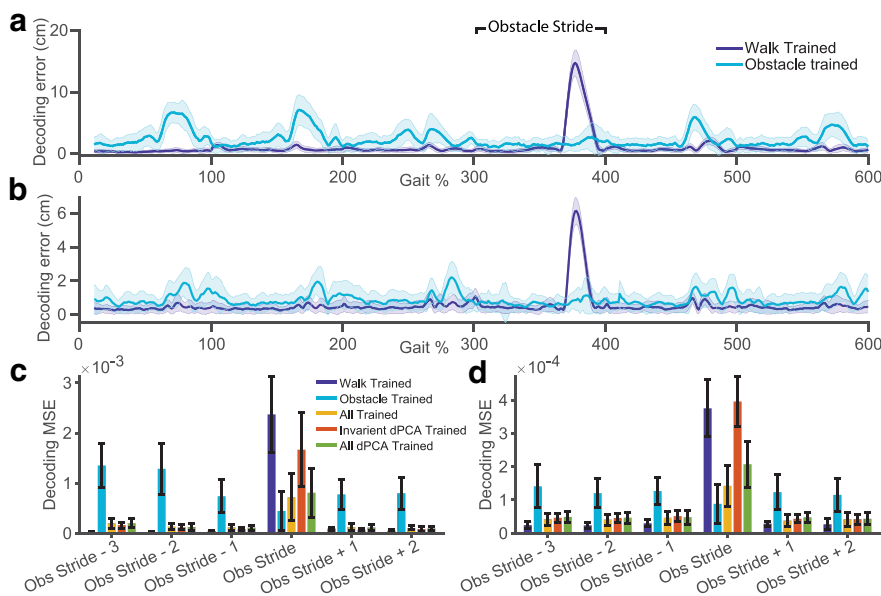


**Figure 10.** Decoding does not generalize across basic walking and obstacle stepping. *a, b*, Error in decoding of the toe height for decoders trained only on the data from the stride before any obstacle movement (stride  $-3$ ; shown in purple) or decoders trained only on data from stride stepping over the obstacle (stride  $0$ ; shown in blue);  $300\text{--}400\%$  represents the stride over the obstacle, and error bars indicate SD. *c, d*, Mean squared error for decoding toe height in each of the strides surrounding the obstacle stride, trained on different sets of training data. “All Trained” indicates a decoder trained on data from all of the strides (tested under cross-validation). “Invariant dPCA Trained” indicates a decoder trained on data from all of the strides, but only using the stride-invariant dPCA components. “All dPCA Trained” indicates a decoder trained on data from all of the strides and using both the stride-invariant and stride-dependent dPCA components. *a, c*, Animal B; *b, d*, animal S.

## Discussion

In this study, we investigated the neural dynamics of primate M1 during simultaneous execution of two movement modalities: basic locomotion and visually guided volitional adjustments in response to an obstacle. Prior research has demonstrated separation of neural activity into distinct subspaces in other contexts. For example, one study has shown that during a forelimb-cycling task, separate subspaces correspond to movement direction,

movement initiation, and rotation (Schroeder et al., 2022). That finding is in agreement with our results, suggesting that different movement parameters may be multiplexed through partitioning into subspaces, although that study did not examine the neural response when the cycling movement trajectory is altered. Another previous study has found different M1 subspaces between rodents walking on a treadmill and rodents pressing a lever, and concluded that separate dynamics emerge in M1 activity when switching between these two behaviors (Miri et al., 2017). However, it is still unknown how these two different aspects of movement are engaged when they have to be conducted together as a single action. Additionally, while the cortical activity during obstacle avoidance has been thoroughly described in cats (Beloozerova and Sirota, 1993*a, b*; Drew et al., 2002, 2008; Beloozerova et al., 2010), this is the first characterization of intra-cortical activity during obstacle avoidance walking in nonhuman primates, an animal model with very dissimilar neuroanatomy and biomechanics from mice and felines. For example, the corticospinal tract makes monosynaptic connections to motor neurons, allowing for more direct control of the musculature, in rhesus macaques (Kuypers, 1964). Here, we found that the subspace-partitioning strategy is used to differentially represent volitional movements and locomotion, behaviors that have been shown to involve different

neural processes and structures, when both types movements are being executed at the same time.

In felines and canines, lesion studies have demonstrated that motor cortex is not necessary for the generation of walking movements (Graham Brown, 1911; Grillner et al., 1997), and the control of basic unobstructed locomotion is thought to be managed by subcortical and spinal circuits (Gerasimenko et al., 2006; McCrea and Rybak, 2008). However, volitional movements, such as reaching, do require cortical input. This extends to complex locomotion, as inactivation and lesion studies have shown that without M1 input, felines and canines are unable to precisely place their limbs on a ladder (Liddell and Phillips, 1944; Beloozerova and Sirota, 1993*a*; Grillner et al., 1997; Metz and Whishaw, 2002; Farr et al., 2006; Friel et al., 2007). In nonhuman primates, numerous studies have also suggested that volitional movements and basic locomotion require different amounts of cortical engagement. In prior studies, macaques were able to walk within days after a lesion to the corticospinal tract, but their ability to carry out fine foot movements were almost completely abolished (Courtine et al., 2005). Similarly, Kuypers (1964) demonstrated that after a pyramidotomy, macaques could still walk and climb up cages, but lost the

ability to make fine dexterous movements (Lemon et al., 2012). These findings suggest that, even in nonhuman primates, regions outside of motor cortex are responsible for, at least partially, generating the movements necessary for locomotion. This is in stark contrast to the essential role that M1 plays during stationary reaching movements. Therefore, the motor cortex of animals carrying out obstacle avoidance



must be able to generate the necessary volitional adaptive movements, while simultaneously taking into account the additional movements being generated by external spinal circuits.

This differential involvement of motor cortex could be instantiated through distinct subpopulations of cells that are activated only during one type of movement. One set of neurons, for example, may be dedicated to monitoring the activity of spinal CPGs, while a separate set of neurons direct the timing and magnitude of the movement over the obstacle. However, we did not find evidence for this in our data; the same neural population was active during both locomotion and volitional gait adjustments. However, our findings indicate that the representation of these two movement modalities are separated within different subspaces.

We used techniques such as dPCA and PLDS to infer the low-dimensional dynamics in M1. We then asked the following: when the animal must carry out a larger movement during the obstacle stride, does the brain modify the whole ongoing neural activity coming from the previous walking strides to carry out the avoidance movement (Fig. 1c)? Our results suggests that this is not the case. Both analyses revealed rotational neural subspaces that are unaffected by the change in movement during obstacle stepping, as well as subspaces that were modulated by the gait adjustment and also necessary for accurate decoding of end point kinematics during the obstacle step. It appears that a subspace in the neural activity emerges that consistently tracks the same cyclic activity throughout, despite large changes in the movement itself, such as a 2–5× increase in the step height. All the variance corresponding to this large change in movement is confined to its own distinct subspace. This subspace separation is not simply the result of the change in kinematics of the movement, because our control dPCA analysis on the kinematics themselves and a simulated dataset revealed very small principal angles.

These different subspaces may correspond to different neural processes involved during obstacle avoidance. One strategy that could be used by the nervous system is to send a feedforward copy of the motor commands generated by the spinal circuits to cortex (Fig. 1a, purple arrow), allowing it to generate the necessary volitional movements within the proper context of the ongoing locomotor sequence. Indeed, it has been previously proposed that the cyclic activity observed in motor cortex during basic locomotion is a reflection of the spinal CPG activity, conveyed through the spinocerebellar tract to the dentate nucleus, and passing through the ventrolateral thalamus before arriving at motor cortex (Massion and Rispal-Padel, 1972; Beloozerova and Sirota, 1998; Marlinski et al., 2012; Beloozerova and Marlinski, 2020). This cyclic activity could potentially be to inform cortex of the state of the limb within the gait cycle, should the need for an adaptive movement arise. After all, the amount of lifting required to clear the obstacle is markedly different depending on whether the leg is in contact with the ground or at the apex of the swing phase.

The existence of the stride-invariant neural modes we observed are in agreement with this hypothesis. The activity within these neural modes remains consistent throughout all gait cycles, even when the kinematics become drastically different during the obstacle stride. These neural modes also exhibit strong rotational dynamics, consistent with the idea that they are induced by the rhythmic activity in spinal CPGs. Additionally, these modes were sufficient for decoding end point kinematics during basic locomotion, but failed during the volitional gait adjustment, suggesting that they do not carry information involving the adjusting movement. However, additional experiments using

causal circuit perturbations will be needed to truly determine the origin of these signals in nonhuman primates.

Meanwhile, the variance related to volitional gait-adjusting movement appear to be contained to a separate set of neural modes. The integration of the visual information along with the calculation of the precise movement required to clear the obstacle may be subserved by these modes. Physically, these modes, which are the linear combinations of the neural activity, may correspond to the synaptic convergence of cortical neurons onto downstream targets. The division of the subspaces we observed is analogous to the output-potent and output-null separation proposed in previous studies (Kaufman et al., 2014; Elsayed et al., 2016; Miri et al., 2017). Lesion studies have demonstrated that motor cortex does not directly control movement during basic locomotion, so the cyclical activity in our stride-independent subspace may be used to inform motor cortex of the phasic activity generated in the spinal cord, without interfering with muscle activation (i.e., the null-space of the stride-dependent subspace). Only when efferent control from M1 is required, such as during the voluntary motion of lifting the leg over the obstacle, does the activity transition into the separate, stride-dependent subspace where the weighted summation of the activity enables the transmission of control signals to the downstream musculature. We hope to test the above conjecture in future studies with more direct experiments.

Finally, our findings have implications for the development of brain-machine interfaces (BMIs) aiming to restore hindlimb functionality for patients with motor deficits. In recent years, advancements have been made in the development of closed-loop systems for restoring walking ability after spinal cord injury (Capogrosso et al., 2016; Donati et al., 2016). These systems use electrophysiology recordings from cortex to drive either spinal stimulation or movement of an exoskeleton, and have demonstrated remarkable success in allowing subjects to recover locomotor ability. These systems currently only aim to restore basic locomotion, and not precise directed leg movements. Our decoding results suggest that future BMIs aiming to restore a wide range of hindlimb movements, including visually adaptive locomotion, should consider including both basic locomotion as well as volitional movements during decoder calibration to achieve optimal performance.

## References

- Aghagolzadeh M, Truccolo W (2014) Latent state-space models for neural decoding. In: Engineering in Medicine and Biology Society (EMBC), 2014 36th annual international conference of the IEEE: date 26–30 Aug. 2014, pp 3033–3036. Piscataway, NJ: IEEE.
- Aghagolzadeh M, Truccolo W (2016) Inference and decoding of motor cortex low-dimensional dynamics via latent state-space models. *IEEE Trans Neural Syst Rehabil Eng* 24:272–282.
- Ames KC, Ryu SI, Shenoy KV (2019) Simultaneous motor preparation and execution in a last-moment reach correction task. *Nat Commun* 10:2718.
- Beloozerova IN, Farrell BJ, Sirota MG, Prilutsky BI (2010) Differences in movement mechanics, electromyographic, and motor cortex activity between accurate and nonaccurate stepping. *J Neurophysiol* 103:2285–2300.
- Beloozerova IN, Marlinski V (2020) Contribution of the ventrolateral thalamus to the locomotion-related activity of motor cortex. *J Neurophysiol* 124:1480–1504.
- Beloozerova IN, Sirota MG (1993a) The role of the motor cortex in the control of accuracy of locomotor movements in the cat. *J Physiol* 461:1–25.
- Beloozerova IN, Sirota MG (1993b) The role of the motor cortex in the control of vigour of locomotor movements in the cat. *J Physiol* 461:27–46.
- Beloozerova IN, Sirota MG (1998) Cortically controlled gait adjustments in the cat. *Ann N Y Acad Sci* 860:550–553.

- Berens P (2009) CircStat: a MATLAB toolbox for circular statistics. *J Stat Softw* 31:1–21.
- Berger M, Agha NS, Gail A (2020) Wireless recording from unrestrained monkeys reveals motor goal encoding beyond immediate reach in frontoparietal cortex. *Elife* 9:e51322.
- Brown TG (1911) The intrinsic factors in the act of progression in the mammal. *Proc R Soc Lond B Biol Sci* 84:308–319.
- Capogrosso M, et al. (2016) A brain-spine interface alleviating gait deficits after spinal cord injury in primates. *Nature* 539:284–288.
- Churchland MM, Cunningham JP, Kaufman MT, Foster JD, Nuyujukian P, Ryu SI, Shenoy KV (2012) Neural population dynamics during reaching. *Nature* 487:51–56.
- Courtine G, Roy RR, Raven J, Hodgson J, McKay H, Yang H, Zhong H, Tuszynski MH, Edgerton VR (2005) Performance of locomotion and foot grasping following a unilateral thoracic corticospinal tract lesion in monkeys (*Macaca mulatta*). *Brain* 128:2338–2358.
- Donati ARC, Shokur S, Morya E, Campos DSF, Moiola RC, Gitti CM, Augusto PB, Tripodi S, Pires CG, Pereira GA, Brasil FL, Gallo S, Lin AA, Takigami AK, Aratana MA, Joshi S, Bleuler H, Cheng G, Rudolph A, Nicoletis MAL (2016) Long-term training with a brain-machine interface-based gait protocol induces partial neurological recovery in paraplegic patients. *Sci Rep* 6:30383.
- Drew T, Doucet S (1991) Application of circular statistics to the study of neuronal discharge during locomotion. *J Neurosci Methods* 38:171–181.
- Drew T, Jiang W, Widajewicz W (2002) Contributions of the motor cortex to the control of the hindlimbs during locomotion in the cat. *Brain Res Rev* 40:178–191.
- Drew T, Andujar J-E, Lajoie K, Yakovenko S (2008) Cortical mechanisms involved in visuomotor coordination during precision walking. *Brain Res Rev* 57:199–211.
- Elsayed GF, Lara AH, Kaufman MT, Churchland MM, Cunningham JP (2016) Reorganization between preparatory and movement population responses in motor cortex. *Nat Commun* 7:13239.
- Farr TD, Liu L, Colwell KL, Whishaw IQ, Metz GA (2006) Bilateral alteration in stepping pattern after unilateral motor cortex injury: a new test strategy for analysis of skilled limb movements in neurological mouse models. *J Neurosci Methods* 153:104–113.
- Foster JD, Nuyujukian P, Freifeld O, Gao H, Walker R, I Ryu S, H Meng T, Murmann B, J Black M, Shenoy KV (2014) A freely-moving monkey treadmill model. *J Neural Eng* 11:046020.
- Friel KM, Drew T, Martin JH (2007) Differential activity-dependent development of corticospinal control of movement and final limb position during visually guided locomotion. *J Neurophysiol* 97:3396–3406.
- Gallego JA, Perich MG, Naufel SN, Ethier C, Solla SA, Miller LE (2018) Cortical population activity within a preserved neural manifold underlies multiple motor behaviors. *Nat Commun* 9:4233.
- Georgopoulos AP, Grillner S (1989) Visuomotor coordination in reaching and locomotion. *Science* 245:1209–1210.
- Gerasimenko YP, Lavrov IA, Courtine G, Ichiyama RM, Dy CJ, Zhong H, Roy RR, Edgerton VR (2006) Spinal cord reflexes induced by epidural spinal cord stimulation in normal awake rats. *J Neurosci Methods* 157:253–263.
- Grillner S, Georgopoulos AP, Jordan LM (1997) Selection and initiation of motor behavior. In: *Neurons, networks and motor behavior* (Stein PSG, Grillner S, Selverston AI, Stuart DG, eds), pp 3–19. Cambridge, MA: MIT.
- He SQ, Dum RP, Strick PL (1993) Topographic organization of corticospinal projections from the frontal lobe: motor areas on the lateral surface of the hemisphere. *J Neurosci* 13:952–980.
- Kaufman MT, Churchland MM, Ryu SI, Shenoy KV (2014) Cortical activity in the null space: permitting preparation without movement. *Nat Neurosci* 17:440–448.
- Kobak D, Brendel W, Constantinidis C, Feierstein CE, Kepecs A, Mainen ZF, Qi X-L, Romo R, Uchida N, Machens CK (2016) Demixed principal component analysis of neural population data. *Elife* 5:e10989.
- Kuypers HGJM (1964) The descending pathways to the spinal cord, their anatomy and function. *Prog Brain Res* 11:178–202.
- Lemon RN, Landau W, Tuttsel D, Lawrence DG (2012) Lawrence and Kuypers (1968a, b) revisited: copies of the original filmed material from their classic papers in *Brain*. *Brain* 135:2290–2295.
- Liddell EGT, Phillips CG (1944) Pyramidal section in the cat. *Brain* 67:1–9.
- Macke JH, Büsing L, Cunningham JP, Yu BM, Shenoy K, Sahani M (2011) Empirical models of spiking in neural populations. In: *Advances in neural information processing systems 24: 25th annual conference on neural information processing systems*, pp 1350–1358. Red Hook, NJ: Curran Associates.
- Macke JH, Büsing L, Sahani M (2015) Estimating state and parameters in state space models of spike trains. In: *Advanced state space methods for neural and clinical data* (Chen Z, ed), pp 137–159. Cambridge: Cambridge UP.
- Marlinski V, Nilaweera WU, Zelenin PV, Sirota MG, Beloozerova IN (2012) Signals from the ventrolateral thalamus to the motor cortex during locomotion. *J Neurophysiol* 107:455–472.
- Massion J, Rispal-Padel L (1972) Spatial organization of the cerebello-thalamo-cortical pathway. *Brain Res* 40:61–65.
- McCrea DA, Rybak IA (2008) Organization of mammalian locomotor rhythm and pattern generation. *Brain Res Rev* 57:134–146.
- Metz GA, Whishaw IQ (2002) Cortical and subcortical lesions impair skilled walking in the ladder rung walking test: a new task to evaluate fore- and hindlimb stepping, placing, and co-ordination. *J Neurosci Methods* 115:169–179.
- Miri A, Warriner CL, Seely JS, Elsayed GF, Cunningham JP, Churchland MM, Jessell TM (2017) Behaviorally selective engagement of short-latency effector pathways by motor cortex. *Neuron* 95:683–696.e11.
- Porter R, Lemon R (1995) *Corticospinal function and voluntary movement*. Oxford: Oxford UP.
- Pruszynski JA, Kurtzer I, Nashed JY, Omrani M, Brouwer B, Scott SH (2011) Primary motor cortex underlies multi-joint integration for fast feedback control. *Nature* 478:387–390.
- Quiroga RQ, Nadasdy Z, Ben-Shaul Y (2004) Unsupervised spike detection and sorting with wavelets and superparamagnetic clustering. *Neural Comput* 16:1661–1687.
- Rodriguez A, Laio A (2014) Clustering by fast search and find of density peaks. *Science* 344:1492–1496.
- Sadtler PT, Quick KM, Golub MD, Chase SM, Ryu SI, Tyler-Kabara EC, Yu BM, Batista AP (2014) Neural constraints on learning. *Nature* 512:423–426.
- Schroeder VE, Perkins SM, Wang Q, Churchland MM (2022) Cortical control of virtual self-motion using task-specific subspaces. *J Neurosci* 42:220–239.
- Scott SH, Cluff T, Lowrey CR, Takei T (2015) Feedback control during voluntary motor actions. *Curr Opin Neurobiol* 33:85–94.
- Truccolo W (2016) From point process observations to collective neural dynamics: nonlinear Hawkes process GLMs, low-dimensional dynamics and coarse graining. *J Physiol Paris* 110:336–347.
- Truccolo W, Eden UT, Fellows MR, Donoghue JP, Brown EN (2005) A point process framework for relating neural spiking activity to spiking history, neural ensemble, and extrinsic covariate effects. *J Neurophysiol* 93:1074–1089.
- Vargas-Irwin C, Donoghue JP (2007) Automated spike sorting using density grid contour clustering and subtractive waveform decomposition. *J Neurosci Methods* 164:1–18.
- Vargas-Irwin CE, Brandman DM, Zimmermann JB, Donoghue JP, Black MJ (2015) Spike train SIMilarity Space (SSIMS): a framework for single neuron and ensemble data analysis. *Neural Comput* 27:1–31.
- Xing D, Aghagholzadeh M, Truccolo W, Bezaed E, Courtine G, Borton D (2019) Low-dimensional motor cortex dynamics preserve kinematics information during unconstrained locomotion in nonhuman primates. *Front Neurosci* 13:1046.
- Yakovenko S, Drew T (2015) Similar motor cortical control mechanisms for precise limb control during reaching and locomotion. *J Neurosci* 35:14476–14490.
- Yin M, Borton DA, Komar J, Agha N, Lu Y, Li H, Laurens J, Lang Y, Li Q, Bull C, Larson L, Rosler D, Bezaed E, Courtine G, Nurmikko AV (2014) Wireless neurosensor for full-spectrum electrophysiology recordings during free behavior. *Neuron* 84:1170–1182.
- Yu BM, Cunningham JP, Santhanam G, Ryu SI, Shenoy KV, Sahani M (2009) Gaussian-process factor analysis for low-dimensional single-trial analysis of neural population activity. *J Neurophysiol* 102:614–635.